REE-assisted U–Pb zircon age (SHRIMP) of an anatectic granodiorite: Constraints on the evolution of the A Silva granodiorite, Iberian allochthonous complexes

P. Castiñeiras [a,*], F. Díaz García [b], J. Gómez Barreiro [a]

[a] Dpto. Petrología y Geoquímica-Instituto de Geología Económica (UCM-CSIC), Facultad de Ciencias Geológicas, Universidad Complutense, 28040 Madrid, Spain
[b] Dpto. Geología, Facultad de Geología, Universidad de Oviedo, 33005 Oviedo, Spain

Keywords:
SHRIMP U–Pb dating
Rare earth elements in zircon
Magmatic arc
Northern Gondwana margin
Iberian massif
Allochthonous complexes
A Silva granodiorite

A B S T R A C T

The A Silva granodiorite is a plutonic body intruded into the metasediments of the upper unit of the Órdenes Complex (Variscan belt, NW Spain). These metasediments represent the middle section of a magmatic arc located in northern Gondwana. The A Silva granodiorite has been classically considered a late Variscan granite. In this work, new field mapping, structural analysis, and SHRIMP U–Pb zircon dating indicate the granodiorite is significantly older. However, the data indicate a concordant age range between 540 and 460 Ma, and therefore CL images are not useful toward the interpretation of the geochronological results. This issue can be unravelled by using the hafnium and rare earth element composition of zircon in the assessment of the age. In this way, we determined that the age distribution was the result of lead loss, rather than a real age scatter or inheritance, and we could obtain a $^{206}Pb/^{238}U$ crystallization age of 510.28 (+1.57, −1.44) Ma using the TuffZirc algorithm.

This age together with the well-preserved field relationships of the host rock permit us to interpret the A Silva granodiorite as multiple sheets intruded into a sequence of metatexitic host rocks after crustal thickening and subsequent decompression that developed coeval with partial melting during the latest stages of a regional extensional event. Taken together with the underlying Monte Castelo gabbro (499 ± 2 Ma), the whole plutonic complex reaches 8 km in thickness and forms an antiformal stack structure in a shear parallel (N–S) cross-section. This structure could be responsible for previously described, localized granulite facies metamorphism.

The presence of a late Cambrian magmatic event has been widely reported in other areas of northern Gondwana and it is related to the opening of the Rheic Ocean.

1. Introduction

The variety of *P–T* conditions where zircon can grow either in metamorphic or in magmatic rocks makes zircon perfectly suited to study the geochronology of tectonically active areas (Kellett et al., 2009; Mattinson et al., 2009; Yui et al., 2009; Fohey-Breting et al., 2010). Single zircon grains can record different geological processes that can be dated by means of an ion microprobe, with the aid of cathodoluminescence (CL) images to recognize different growth zones (Vavra et al., 1996; Kempe et al., 2000; Rubatto and Gebauer, 2000; Corfu et al., 2003). However, traditional CL-assisted dating is insufficient in the correct linkage between geochronological data and geological processes in complex zircons from such active areas. This is because zircon growth zones with similar CL features could correspond to different magmatic and/or metamorphic events that can occur in a short time span. If we are not able to distinguish each magmatic and metamorphic event, and link them with their corresponding age, we end up with a spurious protracted age distribution. In these cases, we need an additional criterion such as the composition of zircon to make the correct interpretation of the ages.

Analytical improvements, together with a growing number of analytical facilities, have made it easier to simultaneously obtain from zircon both geochronological and chemical data, especially the rare earth elements (REE). These improvements have led to the recognition of certain compositional patterns useful to unambiguously link each zircon growth zone with a specific petrogenetic process, whether it be metamorphic (Rubatto, 2002; Whitehouse and Platt, 2003; McClelland et al., 2006; Chen et al., 2010) or magmatic (Gagnevin et al., in press). The petrogenetic information provided by the zircon composition is particularly useful when interpreting a complex age dataset. Thus, the age spread observed in a sample could be attributable to a real age scatter, an inherited component, or to lead (Pb) loss (Coleman et al., 2004; McClelland et al., 2006). Additionally, using this methodology on metamorphosed igneous rocks, it is possible to distinguish non-obvious inherited (i.e., detrital zircon from a sedimentary protolith that are not

* Corresponding author. Tel.: +34 91 394 4908; fax: +34 91 544 2535.
E-mail addresses: castigar@geo.ucm.es (P. Castiñeiras), jugb@usal.es (J.G. Barreiro).

abraded by transport) or metamorphic zircons from those grains that are grown during magmatism.

In the present paper, we use this new approach (REE-assisted zircon dating) to interpret the age distribution obtained in zircons from the A Silva granodiorite. Additionally, the well-preserved intrusive contacts and the general weak deformation in the A Silva granodiorite make it a good tectonic marker that enables us to better understand the relationships among its intrusion and the development of the regional foliation, the generalized top-to-the-NNW shearing and the partial melting processes operating in the metasedimentary country rocks. This leads us to the recognition of a transitory stage of vertical decoupling between the upper and intermediate levels and the lower levels of the arc during its tectonic evolution.

We also first show through field mapping, structural analysis and U–Pb zircon dating that the A Silva granodiorite is older than previously thought, and it is related to a Cambrian–Ordovician arc developed in the northern margin of Gondwana (Gómez Barreiro et al., 2007). This arc drifted away from the continent, giving rise to the Rheic Ocean (Bozkurt et al., 2008; von Raumer and Stampfli, 2008; Nance, in press).

Finally, we consider the general implications of our study for the characterization of the type, timing, and kinematics of the tectonic processes that contributed to the exhumation of the orogenic root generated in the Gondwana continental margin during Cambrian–Ordovician times.

2. Geological background

Preserved as megaklippen in the core of open synforms, the allochthonous complexes occupy the highest structural position in the Variscan belt of the NW Iberian massif (see Martínez Catalán et al., 2009, and references therein). These complexes include a number of allochthonous slices that appear well represented in the largest, the Órdenes Complex (Fig. 1). These slices have been grouped into three main units: named from bottom to top; the basal units, the ophiolitic units (representing the Variscan suture), and the upper units. The basal and ophiolitic units record a westward oceanic subduction (Díaz García et al., 1999a; Sánchez Martínez et al., 2007; Gómez Barreiro et al., 2010) that evolved to continental subduction of the Gondwanan continental margin during Devonian to Early Carboniferous times (Arenas et al., 1995; Martínez Catalán et al., 2007, 2009).

The upper unit is tectonically emplaced above the ophiolitic unit and it presents increasing petrological evidence suggesting that it was generated in an arc environment of the Gondwana continental margin (e.g., Abati et al., 1999; 2003; Fernández Suárez et al., 2003; Andonaegui et al., 2002; Puelles et al., 2005). This arc was separated from Gondwana during the Early Ordovician, starting to drift towards the north at the same time of the opening of the Rheic Ocean (Gómez Barreiro et al., 2007; Martínez Catalán et al., 2009). During the Early Devonian, the upper unit was emplaced over the Gondwana continental margin at the top of the Variscan pile (e.g., Díaz García et al., 1999a). This main tectonic process allows us to directly examine different levels of an arc-derived terrane that would originally have represented an arc crust nearly 55 km thick, according to paleopressure estimates (e.g., Gil Ibarguchi et al., 1999; Arenas and Martínez Catalán, 2002; Puelles et al., 2005). This crustal ensemble is now strongly reduced to approximately 12 km in thickness and it can be further divided into three additional units with contrasting tectonometamorphic evolution, exhumed from different depths, and separated by extensional detachments that from bottom to top are (Martínez Catalán et al., 2002): the high-pressure and high-temperature unit (HP–HT, with remnants of the lower crust and upper mantle), the intermediate-pressure unit with intermediate to high-temperature (IP–IHT, a section of the middle crust) and the intermediate-pressure unit with low-temperature (IP–LT, representing the upper crust).

The HP–HT, upper units consist of high-pressure mafic to felsic granulites, eclogites, and high-pressure gneisses with closely related ultramafic massifs. Most of the mafic rocks are metagabbros of tholeiitic composition. Their geochemical signature has been compared to MORB (Gil Ibarguchi et al., 1990) and geochemical studies on the ultramafic rocks from the Cabo Ortegal outcrops are consistent with the hypothesis that these rocks were generated in an arc setting (Moreno et al., 2001; Santos Zalduegui et al., 2002).

Fabric studies of the main foliation (e.g., Engels, 1972; Ábalos, 1997) demonstrate that eclogite and granulite rocks underwent a regional intense ductile deformation during the highest pressure conditions, followed by widespread development of an amphibolite facies foliation related to their continued exhumation. Later during the Variscan Orogeny progress, isoclinal folds and thrusts under epizonal conditions (e.g., Martínez Catalán et al., 2002; Gómez Barreiro et al., 2007) reworked the whole ensemble.

The age of the HP–HT metamorphism in the allochthonous complexes is a matter of intense debate which will be summarized as follows. A Precambrian age was proposed, based only on the tectonic complexity (e.g., Ribeiro et al., 2007). On the basis of U–Pb zircon data, some authors have proposed a Late Cambrian–Early Ordovician age (ca. 480–495 Ma; Peucat et al., 1990; Fernández Suárez et al., 2002; 2007); whereas others favor a roughly Middle Devonian age (ca. 380–390 Ma; Schafer et al., 1993; Santos Zalduegui et al., 1996; Ordoñez Casado et al., 2001; Roger and Matte, 2005).

The IP–IHT (intermediate-pressure, intermediate- to high-temperature) upper unit consists of a metasedimentary sequence, locally named the O Pino unit, which is dominated by staurolite–kyanite schists and sillimanite–biotite paragneisses (Abati et al., 2003; Castiñeiras, 2005; Gómez Barreiro, 2007). Late Cambrian metaplutonic massifs, such us the Monte Castelo gabbro and the Corredoiras orthogneiss, occur near the base of the unit, together with a number of differently sized gabbroic and granodioritic plutonic bodies. The Monte Castelo gabbro, cropping out to the west of the Órdenes Complex, is the largest and is a massive two-pyroxene gabbro with a tholeiitic character very similar to those of island arc tholeiites (Andonaegui et al., 2002). Under the microscope, textures vary from granular to intergranular and ophitic. The presence of olivine and the common ophitic textures indicate a relatively shallow emplacement.

The Corredoiras orthogneiss is a large granodioritic massif with minor tonalitic and mafic rocks that crops out in the eastern part of the Órdenes Complex. It exhibits a porphyritic texture with alkali feldspar and plagioclase as porphyroclasts in a coarse-grained matrix. The Corredoiras orthogneiss and the related lithologies define a high-K calc-alkaline series, and tectonic discrimination diagrams based on immobile elements suggest a volcanic-arc setting (Andonaegui et al., 2007).

The Corredoiras orthogneiss has been affected by intense top-to-the-north shearing, developing hectometre-thick shear zones within the body and in the basal part that brought it into contact with the underlying HP–HT Sobrado unit (González Cuadra, 2007). The structure responsible for its final emplacement above the ophiolitic unit is also a shear zone developed under greenschist facies conditions and located in its eastern part, where top-to-the-SE kinematic criteria have been obtained (Díaz García et al., 1999b).

Ages belonging to these two main plutonic bodies (ID-TIMS U–Pb in zircon; 499 ± 2 Ma for the Monte Castelo gabbro and 500 ± 2 Ma for the Corredoiras orthogneiss, Abati et al., 1999) confirm that voluminous tholeiitic and calc-alkaline magmatism had a peak at around 500 Ma, and was shortly followed by the development of shear zones. In the basal section of the Monte Castelo gabbro, this shearing was developed under granulite facies conditions and recorded a pressure increase of 2–4 kb (Abati et al., 2003). The shearing was first indirectly dated using U–Pb in monazites from the host high-grade metasediments that yielded an age between 493 and 498 Ma (Abati et al., 1999). More recently, an age of 483 ± 4 Ma was

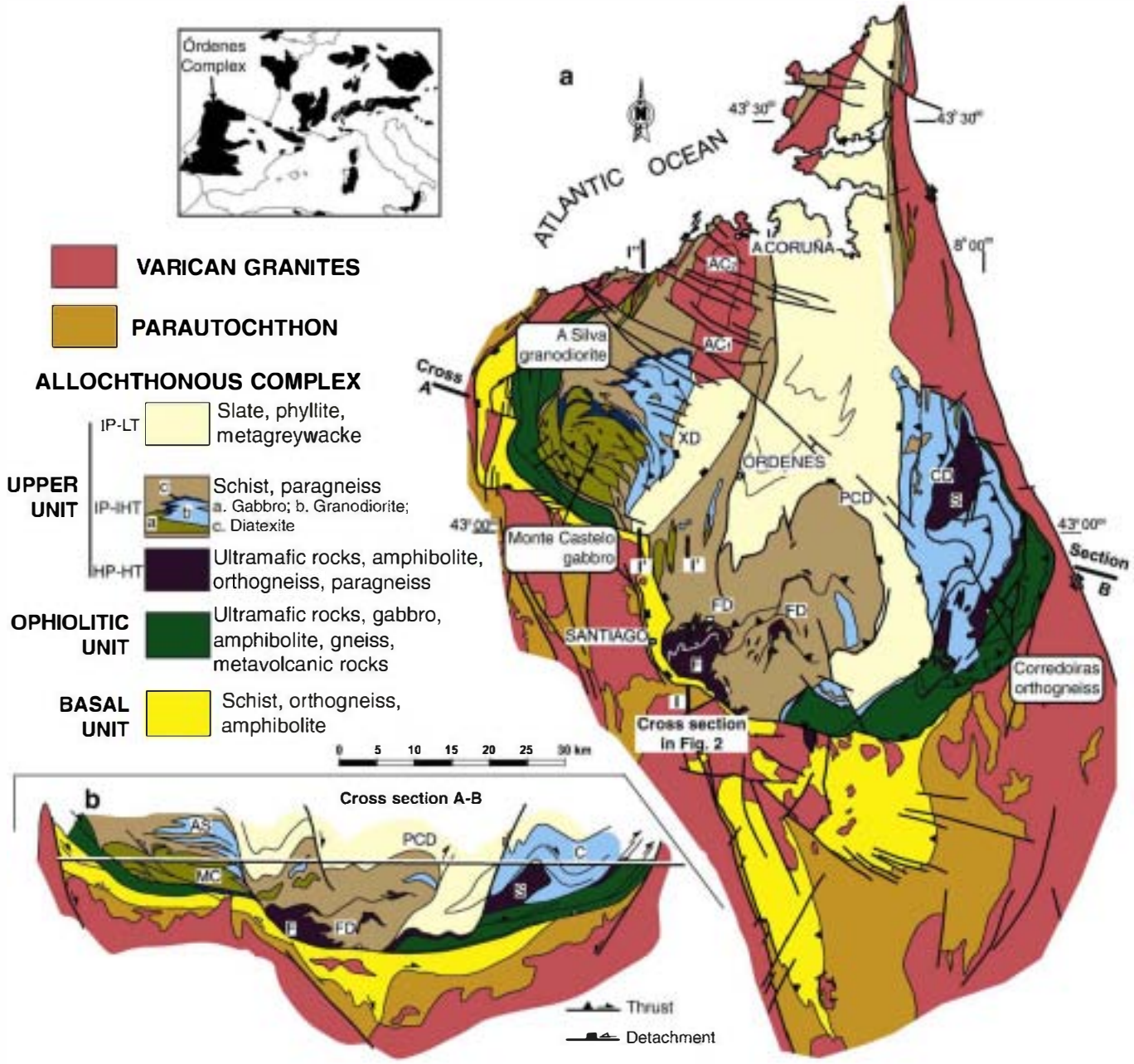

Fig. 1. Geological map (a), and cross-section (b) of the Órdenes Allochthonous Complex with their units and main lithologies. Abbreviations: AC1, A Coruñagranodiorite, porphiritic external facies; AC2, A Coruñagranodiorite central facies; CD, Corredoiras detachment; F, Fornás HP–HT massif; FD, Fornás detachment; PCD, Ponte Carreira detachment; S, Sobrado HP–HT massif; XD, Xesteda detachment.

obtained on metamorphic rims of zircon from a mafic granulite using the SHRIMP (Abati et al., 2007).

In the south of the study area (Fig. 1), the Fornás detachment brought the Fornás and Arinteiro HP–HT granulites from the footwall into contact with the metasediments and gabbroic to granodioritic rocks of the hangingwall that belong to the upper IP–IHT unit (Gómez Barreiro et al., 2007). The hangingwall metasediments were equilibrated under medium-pressure and high-temperature conditions, developing synkinematic leucosomes of granite–granodiorite composition, whereas the granulite rocks from the footwall underwent widespread development of amphibolite facies foliation related to their continued exhumation.

The mylonitic fabrics related to the Fornás detachment were dated by $^{40}Ar/^{39}Ar$ laserprobe incremental heating experiments. The plateau ages obtained for hornblende cluster around 420 Ma (Gómez Barreiro et al., 2006), which are interpreted as the minimum cooling age (below 525 °C), and the upper age-limit for the HP–HT event itself, supporting a polyorogenic origin for the upper units.

The IP–LT (intermediate-pressure, low-temperature) upper unit occupies the top of the upper unit and consists of a package of metapelites and metagreywackes where deposition, folding and intrusion of mafic dikes occurred in a short time span from 520 to 510 Ma (Fernández Suárez et al., 2003; Fuenlabrada et al., 2010; Díaz García et al., 2010). The lower contact with the IP upper units is the Ponte Carreira top-to-the-north extensional detachment (PCD, in Fig. 1). Mylonitic muscovites from the PCD were dated by $^{40}Ar/^{39}Ar$ laserprobe, yielding a cooling age of 371 Ma (Gómez Barreiro et al., 2006).

3. The structure of the A Silva granodiorite

Field work led us to distinguish between the A Silva and the A Coruña granodiorites, previously considered as a single plutonic body (Fig. 1). The latter is a large granodiorite to granite intrusion with a trapezoid shape (in map view), which crosscuts upright regional Variscan folds. Two main petrographic types were recognized on the basis of texture and modal composition, following a classical normal zoning pattern (Bellido et al., 1987). A porphyritic external facies occupies the largest area and is characterized by K-feldspar megacrysts (AC_1 in Fig. 1), whereas coarse-grained, non-porphyritic two-mica granite, including fine- to medium-grained, two-mica leucogranite, are located in the core of the pluton (AC_2 in Fig. 1). Magmatic foliation identified by the alignment of feldspar megacrysts is sometimes observed, and the presence of a vertical tectonic foliation is restricted to its margins in the northern area, associated with cataclastic rocks. Thus, the structural features of the A Coruña granodiorite are similar to other Carboniferous granites in this part of the Variscan belt, where they appear undeformed or locally affected by a vertical S–C type foliation related to strike-slip shearing (e.g., Iglesias and Choukroune, 1980).

In contrast, the A Silva granodiorite exhibits a coarse-grained porphyritic texture with Pl and Kfs centimetre-scale megacrysts in a coarse-grained matrix with abundant biotite aggregates and microgranite to tonalite enclaves, thus giving it a restitic appearance. The granodiorite also contains a number of elongate metasedimentary enclaves, the western contact being delineated by the presence of several pieces of wall rock embedded in the pluton that are nearly concordant with the metasedimentary country rocks. The A Silva granodiorite exhibits a flat-lying S–C type foliation that is folded into an upright open antiform with a fold axis gently plunging to the NE (Fig. 1). Its eastern limb is transected by the Xesteda east-dipping normal fault (XD in Fig. 1), which brought it into contact with the IP–LT metasedimentary sequence of the upper unit.

Metasedimentary country rocks of the upper IP–IHT zone of the upper unit consist of amphibolite facies schists and paragneisses, where the gradual transition from metatexite to diatexite can be observed close to the A Silva granodiorite. Regional foliation of the metasediments is marked by quartz- and micaceous-rich millimetre-scale stripes with microscopic evidence of having evolved from a crenulation cleavage S2. Frequently, the S2 planes are associated to spaced C and C′ shear planes, producing a sigmoidal shape to the foliation. Commonly, the metasediments appear as metatexites characterized by centimetre-scale melt segregations (leucosomes) along the foliation planes to form stromatitic migmatite, but also with small pods of post-S2 leucosomes accumulated in dilated sites developed during shearing.

Close to the A Silva granodiorite, at its western and upper contacts, an irregular diatexite envelope has been mapped (Fig. 1). It is characterized by the disintegration of the S2 foliation from the host rocks and the development of raft-rich schlieren and heterogeneous diatexites with some ghost metatexitic layering preserved. Massive diatexites can also be found, which contain plagioclase and K-feldspar phenocrysts and a relatively uniform texture interrupted by the presence of centimetre-scale clasts of stromatitic migmatite. Thus, the above described field relationships suggest that partial melting took place synchronously with the final stages of the S2 foliation development, subsequent shearing, and granodioritic intrusion.

Most of the A Silva granodiorite outcrops show a weak foliation defined by the flattening of biotitic aggregates, the incipient development of quartz and feldspar ribbons and the rotation of feldspar megacrysts. An S–C type foliation can be observed in its basal sheet and in narrow bands of the interior of the pluton, where it acquires a gneissic fabric. The stretching lineation on C planes is subhorizontal and it has a roughly N30W trend and allows us to deduce a top-to-the-NNW shearing. To a lesser extent, especially in the southern end of the granodioritic massif, the opposite sense of shear has also been found.

According to the geometry of the western contact, field observations and to the presence of several metasedimentary xenoliths, the A Silva granodiorite consists of multiple laminar bodies that intruded a sequence of metatexitic country rocks, subsequently affected by top-to-the-NNW shearing and later folded into an upright antiform.

Taken together with the underlying Monte Castelo gabbro and in absence of detailed petrological and geochemical analysis, it could be envisioned that the whole ensemble constitutes a plutonic complex that reached, in its present configuration, near8 km in thickness. Though the initial configuration of this complex is impossible to ascertain, it can be suggested that the main lens-shape was acquired as a consequence of being dismembered into a number of superposed tectonic sheets, altogether depicting a duplex, and forming an antiformal stack structure that is represented in a composite section in Fig. 2. This configuration could be responsible for the pressure increase recorded in the granulitic shear zones located at the base of the Monte Castelo gabbro. If this interpretation were correct, the granulite facies metamorphism described in the Monte Castelo gabbro (Abati et al., 2003) would be the result of a localized metamorphism originated by magmatic underplating, rather than the result of a regional metamorphism developed during a crustal thickening episode.

4. U–Pb, REE and Hf SHRIMP analysis

4.1. Sample description

Two samples from the A Silva granodiorite, A Silva-1 and A Silva-2, were selected for SHRIMP analysis that includes U–Pb geochronology, and REE (rare earth elements) and Hf determinations in zircon. The first sample was collected near the A Coruña granodiorite, in the northern outer area of the pluton, to trace its extent as far as possible. The second sample was selected from a type locality at the internal part of the pluton.

Zircon separation was carried out at the Universidad Complutense (Madrid) following standard techniques, including crushing, pulverizing, sieving, Wilfley table, magnetic separator and heavy liquid (methylene iodide). Zircons from both samples have similar characteristics; they are colorless or light brown, with scarce mineral or fluid inclusions. Most of the grains are elongated dipyramidal prisms with simple habit and high length-to-width ratios, less predominant and smaller in A Silva-2. In stubbier grains, it is possible to recognize xenocrystic cores. Big (0.1 mm wide, 0.3 mm long), colored, multifaceted grains are common and they are usually broken. Rounded zircons or grains with signs of surface abrasion are also present. In the final mineral separate, sulfide grains (mainly pyrite and chalcopyrite) and apatite are common. Apatite is easily distinguished from zircon because of its duller surface, caused by its lower refractory index, and its bigger size.

The zircon grains were handpicked under a binocular microscope at the Stanford-US Geological Survey micro analytical center (SUMAC). Zircon with the most transparent habit and highest length-to-width ratios were selected to avoid inherited and metamorphic grains as much as possible. Two aliquots of A Silva-1 and one of A Silva-2 were mounted separately on glass slides with a double-sided adhesive in 1×6 mm parallel rows together with some grains of zircon standard R33 (Black et al., 2004) and set in epoxy resin. After the resin was cured, the mounts were ground down to expose their central portions by using 1500 grit wet sandpaper and polished with 6 μm and 1 μm diamond abrasive on a lap wheel. Prior to isotopic analysis, the internal structure, inclusions, fractures and physical defects were identified with transmitted and reflected light on a petrographic microscope, and with cathodoluminescence (CL) on a JEOL 5600LV scanning electron microscope. Following the analysis, secondary electron images were taken to determine the exact location of the spots.

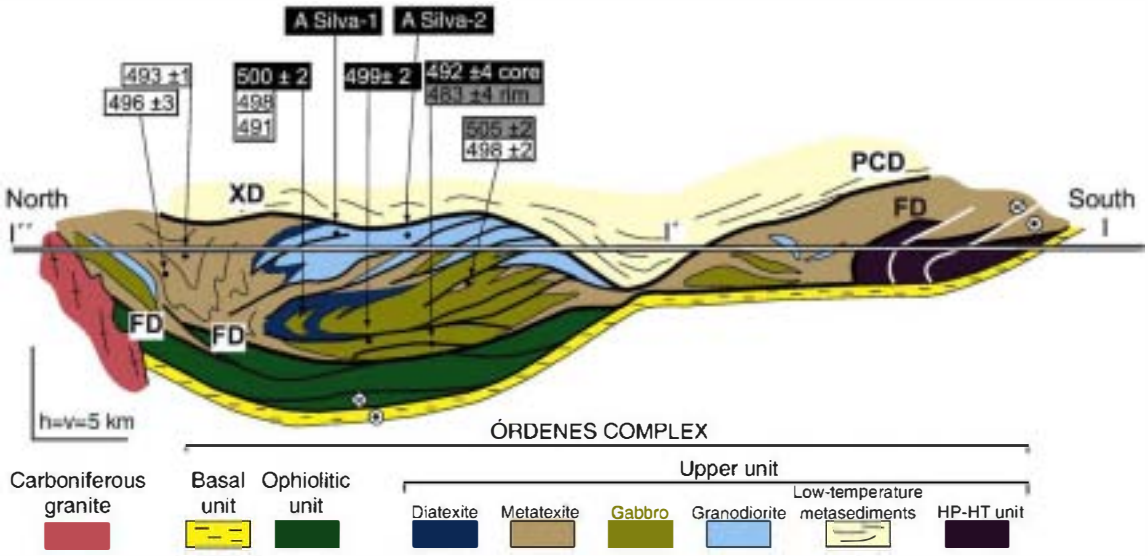

Fig. 2. Synthetic cross-section, approximately parallel to the inferred tectonic transport direction, showing the relationships between the main extensional detachments and the antiformal stack developed in the gabbroic and granodioritic plutonic complex. Abbreviations as in Fig. 1. Zircon U–Pb protolith ages are shown in black boxes, zircon U–Pb metamorphic ages in grey boxes and U–Pb monacite ages in white boxes. Hornblende $^{40}Ar/^{39}Ar$ ages underlined.

Cathodoluminescence images of zircons from the first A Silva-1 aliquot (Fig. 3) display moderately luminescent oscillatory zoning. In some zircon grains, internal zones appear truncated and surrounded by additional oscillatory zones and the internal zones may represent an inherited component. Discontinuous, poorly luminescent rims with faint oscillatory zoning may occur in several grains. Zircons from the

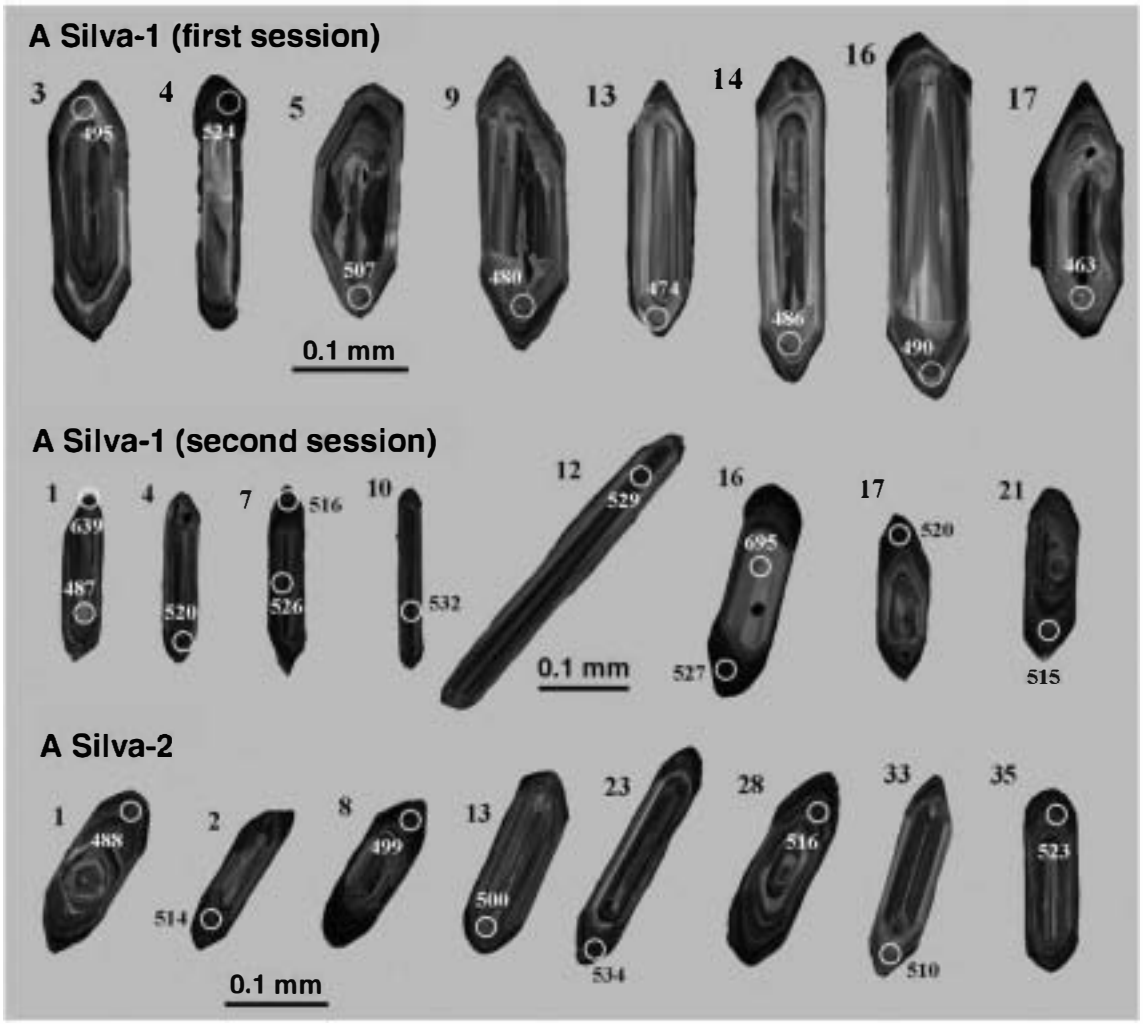

Fig. 3. Cathodoluminescence images for selected zircons from samples (a) A Silva-1, first aliquot, (b) A Silva-1, second aliquot, and (c) A Silva-2.

second A Silva-1 aliquot are slightly longer but show similar CL features (Fig. 3), i.e., some possible inherited xenocrystic cores overlain by oscillatory-zoned zircon that is extended to the outer grain surface, and usually gets darker and fainter to the rim. Zircons from A Silva-2 are smaller but they share the same CL characteristics (Fig. 3).

4.2. Analytical techniques

U–Th–Pb, REE and Hf analyses of zircon were conducted on the Bay SHRIMP-RG (sensitive high resolution ion microprobe-reverse geometry) operated by the SUMAC facility (Stanford University-USGS microanalysis center) during three analytical sessions in May and September 2008.

U–Th–Pb analytical procedures for zircon dating follow the methods described in Williams (1997). Secondary ions were generated from the target spot with an O^{2-} primary ion beam varying from 4 to 6 nA. The primary ion beam produced a spot with a diameter of ~25 μm and a depth of 1–2 μm for an analysis time of 12–13 min. Data for each spot were collected utilizing five-cycle runs through the mass stations, and the counting time for ^{206}Pb was increased according to the Paleozoic age of the samples to improve counting statistics and precision of the $^{206}Pb/^{238}U$ age. The isotopic compositions were calibrated against R33 ($^{206}Pb^*/^{238}U = 0.06716$, equivalent to an age of 419 Ma, Black et al., 2004) which was analyzed every fourth analysis. Calibration errors for $^{206}Pb/^{238}U$ ratios of R33 for the different analytical sessions were 0.91%, 0.64%, and 0.49% (2σ). The calculated external errors were incorporated when data from all sessions and mounts were compiled together.

Data reduction was carried out using Squid software (Ludwig, 2002) which follows the methods described by Williams (1997), and Ireland and Williams (2003), and Isoplot software (Ludwig, 2003) was used to create the graphs. All the ages are reported based on $^{206}Pb/^{238}U$ ratios corrected from common Pb using the ^{207}Pb method. The Pb composition used for initial Pb corrections ($^{204}Pb/^{206}Pb = 0.0554$, $^{207}Pb/^{206}Pb = 0.864$ and $^{208}Pb/^{206}Pb = 2.097$) was estimated from Stacey and Kramers (1975). Analytical results are presented in Table 1, and plotted in Fig. 4.

La to Yb and Hf were measured concurrently with the U–Th–Pb analyses as additional masses on each pass through the mass range. In the second and third sessions, two more peaks were included in the procedure (Y and Lu), whereas Ce was not analyzed in the A Silva-1 second session. The concentration of U, Th, Hf and REE were calibrated using an in-house zircon standard (MAD, see concentrations in Table 2) and are reproducible at 2–4% (1σ), except for La (15%) because of its typical low concentration. Pr was calculated from its neighbor elements because CeH cannot be resolved from the Pr peak and contributes significantly to the counts at Pr^{141}, given the low abundance of Pr and the relatively much high Ce concentration.

4.3. U–Pb results

The eighty-three analyses performed on 73 zircon grains suggest that both A Silva samples are equivalent, and the data is accordingly considered together henceforth. After an initial appraisal of the data, a couple of analyses were ruled out in the discussion of the crystallization age because of their evident inherited nature (A Silva-1, #16.2) or high common Pb content (A Silva-2, #5). Moreover, some zircons from the second A Silva-1 aliquot exhibit a behavior that defies conventional schemes of interpretation as younger ages were obtained for inner rather than outer areas of grains. Several possibilities were considered to explain this particularity, including a failure in the calibration, extreme Pb-loss in the zircon cores owning to radiation damage, an analytical bias due to high U content in the zircon rims (Butera et al., 2001), or heterogeneity of the zircon with depth as the oxygen beam excavates the surface during analysis. However, none of these possibilities seem to apply in this case and we decided to discard those analyses (1, 2, 3, 5, 8, 13 and 15) in the subsequent discussion. The remaining 67 spots represent oscillatory zones, disregarding their luminescence, avoiding evident xenocrystic cores and homogeneous non-luminescent rims. The results show a rough correlation between luminescence and U content, which varies from 150 to 1750 ppm, even though most of the zircons have moderate U concentrations (lower than 400 ppm). The analyses define an apparent concordant age range between 540 and 460 Ma along concordia on a Tera–Wasserburg plot (Fig. 4). Th/U ratios display a wide range of values, 0.04 to 0.95, and show two distinct trends when plotted against the $^{206}Pb/^{238}U$ age (Fig. 5). Most of the analyses define a gentle slope, with a greater Th/U range in younger zircons, whereas at least seven analyses from the second A Silva-1 aliquot exhibit a steeper slope (analyses #5.1, 7.1, 9, 10, 11, 12 and 14). These seven analyses were obtained from central areas of oscillatory zoning in apparently simple zircons (Fig. 3). However, in the light of this plot, it is likely that they are inherited zircons, and therefore will be omitted from any further discussion of the A Silva granodiorite crystallization age. Still, obtaining an age with such smooth variation in the data is not straightforward and it requires a coupled assessment with the REE and Hf composition of the zircons.

4.4. Zircon REE and Hf composition

Chondrite-normalized REE plots are presented in Fig. 6, using values from Anders and Grevesse (1989) modified by Korotev (1996). We have plotted sixty-one A Silva analyses, together with zircon standard R33 data for comparison. In general, all samples have REE patterns characteristic of magmatic zircon (Hoskin and Schaltegger, 2003; Hanchar and van Westrenen, 2007). In the A Silva zircons, La contents are usually low, ranging from 0.003 to 0.5 ppm. Higher values (0.5–15 ppm) are commonly associated with high U contents and could reflect metamictization of the zircon (Belousova et al., 2002; Hoskin, 2005). Ce/Ce^* positive anomalies are variable, from 1 to 21, with the lowest values largely influenced by light (L) REE concentrations. This anomalous Ce content is usually interpreted as the result of the oxidation state of the original magma, which favors Ce^{4+} versus Ce^{3+} (Hoskin and Schaltegger, 2003), although fractionation of other minerals that predominantly take Ce^{3+} is also possible (Wooden et al., 2006). The patterns show a pronounced negative Eu anomaly ($Eu/Eu^* = 0.02–0.05$), with higher values in the analyses with higher LREE contents. Ce and Eu oxidation state is dependent on oxygen fugacity; however, there is no simple correlation between both anomalies because plagioclase growth strongly influences Eu^{2+} availability in the magma. Heavy (H) REE values show a variation between $Dy_N = 100–3000$ and $Yb_N = 1000–10{,}000$, and the patterns reveal a uniform moderately fractionated shape, with most of the Yb/Gd values ranging between 10 and 20.

Comparatively, zircon standard R33 has lower and more homogeneous La concentration (0.005–0.25 ppm). Ce/Ce^* anomalies are higher with values ranging from 10 to 100. The negative Eu/Eu^* anomaly is shallower and more homogeneous (~0.30). HREE vary between $Dy_N = 110–2100$ and $Yb_N = 850–8000$, and display a more fractionated and variable pattern than the A Silva zircons with Yb/Gd values ranging between 10 and 40.

5. Discussion

5.1. Petrogenesis of the A Silva granodiorite: the zircon REE approach

Taking into account the zircon REE contents and various elemental ratios, some petrogenetic aspects can be suggested for the A Silva granodiorite. Wooden et al. (2006) and Lowery Claiborne et al. (2006) have determined that there are three excellent monitors of magma evolution by fractional crystallization during zircon growth, namely, Yb/Gd, Th/U and Hf.

Table 1
U–Th–Pb SHRIMP analytical data for zircons from the A Silva granodiorite.

Spot number and description[a]		Common 206Pb (%)[b]	U (ppm)	Th (ppm)	Th/U	^{207}Pb corrected		Uncorrected ratios		^{204}Pb corrected ratios	
						^{206}Pb/^{238}U age	^{206}Pb*/^{238}Uc	^{238}U/^{206}Pb	^{207}Pb/^{206}Pb	^{238}U/^{206}Pb*c	^{207}Pb*/^{206}Pb*
A Silva 1: Metagranodiorite (first aliquot). UTM: 540003, 4780000, 440											
1	o	0.19	436	53	0.13	472.6 ± 5.6	0.0761 ± 0.0010	13.12 ± 1.3	0.0580 ± 1.6	13.14 ± 1.3	0.0572 ± 1.8
2	o	−0.06	258	133	0.53	489.6 ± 6.2	0.0789 ± 0.0011	12.68 ± 1.4	0.0564 ± 2.0	12.68 ± 1.4	0.0564 ± 2.0
3	o	−0.01	209	36	0.18	495.0 ± 6.5	0.0798 ± 0.0012	12.53 ± 1.5	0.0570 ± 2.2	12.55 ± 1.5	0.0558 ± 2.5
4	o	−0.10	1748	84	0.05	524.1 ± 5.7	0.0847 ± 0.0011	11.82 ± 1.2	0.0570 ± 0.8	11.82 ± 1.2	0.0572 ± 0.8
5	o	−0.06	252	50	0.21	507.2 ± 6.5	0.0819 ± 0.0012	12.22 ± 1.4	0.0569 ± 2.1	12.24 ± 1.4	0.0562 ± 2.3
6	o	0.05	188	33	0.18	496.8 ± 6.3	0.0801 ± 0.0012	12.48 ± 1.4	0.0576 ± 2.0	12.49 ± 1.4	0.0566 ± 2.2
7	o	0.19	380	42	0.11	475.7 ± 5.7	0.0766 ± 0.0010	13.03 ± 1.3	0.0582 ± 1.4	13.05 ± 1.3	0.0573 ± 1.6
8	o	0.19	821	154	0.19	479.2 ± 5.3	0.0772 ± 0.0010	12.93 ± 1.2	0.0582 ± 1.0	12.94 ± 1.2	0.0579 ± 1.0
9	o	−0.06	218	37	0.18	480.2 ± 6.0	0.0773 ± 0.0011	12.94 ± 1.4	0.0562 ± 1.9	12.96 ± 1.4	0.0547 ± 2.4
10	o	0.17	239	37	0.16	474.4 ± 5.9	0.0764 ± 0.0011	13.07 ± 1.4	0.0579 ± 1.9	13.07 ± 1.4	0.0579 ± 1.9
11	o	0.45	268	63	0.24	474.2 ± 5.9	0.0763 ± 0.0011	13.04 ± 1.4	0.0602 ± 1.6	13.06 ± 1.4	0.0589 ± 2.0
12	o	0.04	185	19	0.10	476.8 ± 6.1	0.0768 ± 0.0011	13.02 ± 1.4	0.0570 ± 2.0	13.03 ± 1.4	0.0563 ± 2.2
13	o	0.67	159	55	0.36	474.1 ± 6.6	0.0763 ± 0.0012	13.01 ± 1.6	0.0620 ± 2.2	13.14 ± 1.6	0.0543 ± 5.4
14	o	−0.37	184	72	0.40	486.0 ± 6.2	0.0783 ± 0.0011	12.82 ± 1.4	0.0539 ± 2.1	12.83 ± 1.4	0.0532 ± 2.3
15	o	−0.03	321	36	0.11	504.8 ± 6.0	0.0815 ± 0.0011	12.28 ± 1.3	0.0571 ± 1.5	12.29 ± 1.3	0.0567 ± 1.6
16	o	−0.07	242	44	0.19	489.9 ± 6.3	0.0790 ± 0.0012	12.67 ± 1.4	0.0564 ± 1.9	12.67 ± 1.4	0.0564 ± 1.9
17	o	0.16	147	66	0.46	462.5 ± 6.2	0.0744 ± 0.0011	13.42 ± 1.5	0.0575 ± 2.4	13.42 ± 1.5	0.0575 ± 2.4
A Silva 1: Metagranodiorite (second aliquot)											
1.1	c	0.22	134	70	0.54	487.3 ± 3.4	0.0785 ± 0.0009	12.71 ± 1.1	0.0587 ± 3.0	12.71 ± 1.1	0.0587 ± 3.0
1.2	r	0.20	464	78	0.17	639.2 ± 2.9	0.1042 ± 0.0008	9.57 ± 0.7	0.0626 ± 2.0	9.62 ± 0.7	0.0585 ± 3.4
2.1	r	0.05	674	71	0.11	519.2 ± 1.6	0.0839 ± 0.0004	11.92 ± 0.5	0.0582 ± 1.3	11.92 ± 0.5	0.0579 ± 1.3
2.2	c	0.00	151	56	0.38	496.4 ± 3.3	0.0800 ± 0.0009	12.49 ± 1.0	0.0572 ± 3.9	12.49 ± 1.0	0.0572 ± 3.9
3.1	r	0.03	561	94	0.17	526.1 ± 1.8	0.0850 ± 0.0005	11.76 ± 0.5	0.0582 ± 1.4	11.77 ± 0.5	0.0574 ± 1.6
3.2	c	0.27	114	41	0.37	486.0 ± 3.5	0.0783 ± 0.0009	12.74 ± 1.1	0.0591 ± 3.1	12.79 ± 1.2	0.0555 ± 4.6
4	o	0.09	495	56	0.12	520.3 ± 2.0	0.0841 ± 0.0005	11.88 ± 0.6	0.0585 ± 1.8	11.90 ± 0.6	0.0573 ± 2.1
5.1	r	−0.05	636	49	0.08	539.5 ± 1.8	0.0873 ± 0.0005	11.46 ± 0.5	0.0579 ± 1.4	11.46 ± 0.5	0.0579 ± 1.4
5.2	c	−0.03	232	52	0.23	522.0 ± 2.7	0.0844 ± 0.0007	11.86 ± 0.8	0.0576 ± 2.2	11.86 ± 0.8	0.0576 ± 2.2
6	o	0.12	360	43	0.12	508.8 ± 2.3	0.0821 ± 0.0006	12.16 ± 0.7	0.0584 ± 2.2	12.16 ± 0.7	0.0584 ± 2.2
7.1	c	−0.06	500	444	0.92	526.3 ± 1.9	0.0851 ± 0.0005	11.76 ± 0.6	0.0574 ± 1.5	11.77 ± 0.6	0.0571 ± 1.5
7.2	r	0.00	612	54	0.09	516.3 ± 1.7	0.0834 ± 0.0005	11.99 ± 0.5	0.0577 ± 1.4	12.01 ± 0.5	0.0563 ± 1.8
8.1	c	0.19	386	45	0.12	518.7 ± 2.1	0.0838 ± 0.0006	11.91 ± 0.6	0.0593 ± 1.7	11.91 ± 0.6	0.0593 ± 1.7
8.2	r	−0.08	1155	83	0.07	529.6 ± 1.2	0.0856 ± 0.0003	11.69 ± 0.4	0.0573 ± 0.9	11.69 ± 0.4	0.0570 ± 1.0
9	o	0.11	271	65	0.25	539.4 ± 2.8	0.0873 ± 0.0007	11.45 ± 0.8	0.0592 ± 2.2	11.46 ± 0.8	0.0579 ± 2.5
10	o	−0.07	425	162	0.40	532.3 ± 2.1	0.0861 ± 0.0005	11.63 ± 0.6	0.0575 ± 1.6	11.64 ± 0.6	0.0566 ± 1.8
11	o	−0.21	135	67	0.51	520.4 ± 3.6	0.0841 ± 0.0009	11.92 ± 1.1	0.0561 ± 2.9	11.92 ± 1.1	0.0561 ± 2.9
12	o	−0.31	348	226	0.67	528.7 ± 2.3	0.0855 ± 0.0006	11.74 ± 0.7	0.0554 ± 1.8	11.75 ± 0.7	0.0544 ± 2.2
13.1	c	−0.39	68	23	0.34	502.2 ± 4.9	0.0810 ± 0.0013	12.39 ± 1.5	0.0541 ± 4.5	12.23 ± 1.7	0.0649 ± 9.0
13.2	r	−0.13	417	54	0.13	530.6 ± 2.5	0.0858 ± 0.0007	11.67 ± 0.7	0.0569 ± 1.7	11.70 ± 0.7	0.0550 ± 2.3
14	o	0.07	298	128	0.44	517.4 ± 2.4	0.0836 ± 0.0006	11.96 ± 0.7	0.0582 ± 2.0	11.96 ± 0.7	0.0582 ± 2.0
15.1	c	−0.53	139	34	0.25	496.4 ± 3.5	0.0801 ± 0.0009	12.56 ± 1.1	0.0529 ± 3.2	12.61 ± 1.1	0.0496 ± 4.8
15.2	r	−0.02	594	41	0.07	517.3 ± 1.7	0.0836 ± 0.0004	11.97 ± 0.5	0.0575 ± 1.3	11.97 ± 0.5	0.0575 ± 1.3
16.1	r	−0.07	780	36	0.05	527.3 ± 1.5	0.0852 ± 0.0004	11.74 ± 0.5	0.0574 ± 1.2	11.74 ± 0.5	0.0574 ± 1.2
16.2	c, inher	−0.42	87	39	0.47	695.6 ± 6.0	0.1139 ± 0.0016	8.81 ± 1.4	0.0591 ± 3.3	8.81 ± 1.4	0.0591 ± 3.3
17	o	−0.12	693	71	0.11	519.5 ± 1.6	0.0839 ± 0.0004	11.93 ± 0.5	0.0567 ± 1.3	11.94 ± 0.5	0.0562 ± 1.4
18	o	0.75	296	45	0.16	511.9 ± 2.5	0.0826 ± 0.0006	12.01 ± 0.7	0.0636 ± 2.6	12.11 ± 0.8	0.0572 ± 4.9
19	o	0.11	625	36	0.06	513.5 ± 1.6	0.0829 ± 0.0004	12.05 ± 0.5	0.0585 ± 1.4	12.06 ± 0.5	0.0578 ± 1.6
20	o	0.01	437	25	0.06	507.0 ± 1.9	0.0818 ± 0.0005	12.22 ± 0.6	0.0575 ± 1.6	12.23 ± 0.6	0.0567 ± 1.7
21	o	−0.20	337	58	0.18	515.2 ± 2.2	0.0832 ± 0.0006	12.04 ± 0.7	0.0560 ± 2.3	12.04 ± 0.7	0.0560 ± 2.3
A Silva 2: Metagranodiorite. UTM: 538749, 4775197, 354											
1	o	0.10	242	41	0.18	486.5 ± 1.3	0.0784 ± 0.0004	12.74 ± 0.6	0.0577 ± 1.5	12.76 ± 0.6	0.0564 ± 1.8
2	o	−0.21	345	55	0.17	513.1 ± 1.2	0.0829 ± 0.0004	12.10 ± 0.5	0.0558 ± 1.3	12.09 ± 0.5	0.0560 ± 1.3
3	o	0.10	245	65	0.27	511.7 ± 1.4	0.0826 ± 0.0005	12.09 ± 0.6	0.0583 ± 1.6	12.13 ± 0.6	0.0559 ± 2.5
4	o	−0.09	657	85	0.13	519.9 ± 0.9	0.0840 ± 0.0003	11.92 ± 0.3	0.0570 ± 1.3	11.91 ± 0.3	0.0573 ± 1.4
5	hcPb	2.13	959	80	0.09	461.2 ± 0.7	0.0742 ± 0.0002	13.20 ± 0.3	0.0735 ± 0.8	13.47 ± 0.3	0.0572 ± 2.7
6	o	0.14	379	51	0.14	497.0 ± 1.1	0.0801 ± 0.0004	12.46 ± 0.4	0.0583 ± 1.2	12.46 ± 0.4	0.0584 ± 1.2
7	o	0.09	393	29	0.08	487.0 ± 1.1	0.0785 ± 0.0004	12.73 ± 0.4	0.0576 ± 1.3	12.73 ± 0.4	0.0577 ± 1.3
8	o	0.13	339	20	0.06	498.2 ± 1.1	0.0803 ± 0.0004	12.43 ± 0.5	0.0582 ± 1.3	12.44 ± 0.5	0.0578 ± 1.4
9	o	0.56	365	40	0.11	510.3 ± 1.2	0.0824 ± 0.0004	12.07 ± 0.5	0.0621 ± 1.3	12.13 ± 0.5	0.0579 ± 2.3
10	o	0.02	1516	55	0.04	521.3 ± 0.8	0.0842 ± 0.0003	11.87 ± 0.3	0.0579 ± 0.6	11.88 ± 0.3	0.0575 ± 0.6
11	o	−0.01	382	31	0.08	517.9 ± 1.2	0.0837 ± 0.0004	11.96 ± 0.5	0.0576 ± 1.3	11.95 ± 0.5	0.0578 ± 1.3
12	o	−0.05	324	67	0.21	518.4 ± 1.3	0.0837 ± 0.0004	11.95 ± 0.5	0.0573 ± 1.4	11.95 ± 0.5	0.0570 ± 1.4
13	o	0.20	176	47	0.27	498.9 ± 1.6	0.0805 ± 0.0006	12.40 ± 0.7	0.0588 ± 1.8	12.41 ± 0.7	0.0583 ± 1.9
14	o	−0.06	859	46	0.06	509.2 ± 0.7	0.0822 ± 0.0002	12.17 ± 0.3	0.0570 ± 0.8	12.17 ± 0.3	0.0569 ± 0.8
15	o	0.01	319	54	0.17	494.5 ± 1.3	0.0797 ± 0.0004	12.54 ± 0.5	0.0571 ± 1.4	12.55 ± 0.5	0.0567 ± 1.5
16	o	−0.07	332	44	0.14	522.3 ± 1.3	0.0844 ± 0.0004	11.86 ± 0.5	0.0573 ± 1.4	11.85 ± 0.5	0.0575 ± 1.4
17	o	−0.30	305	25	0.08	510.5 ± 1.3	0.0824 ± 0.0005	12.17 ± 0.5	0.0551 ± 1.5	12.17 ± 0.5	0.0553 ± 1.5
18	o	−0.15	276	42	0.16	496.9 ± 1.3	0.0801 ± 0.0004	12.50 ± 0.5	0.0559 ± 1.5	12.51 ± 0.5	0.0552 ± 1.6
19	o	−0.06	348	35	0.10	519.1 ± 1.2	0.0839 ± 0.0004	11.93 ± 0.5	0.0572 ± 1.3	11.93 ± 0.5	0.0574 ± 1.3
20	o	0.09	541	43	0.08	496.6 ± 0.9	0.0801 ± 0.0003	12.48 ± 0.4	0.0579 ± 1.4	12.47 ± 0.4	0.0580 ± 1.4

(continued on next page)

Table 1 (*continued*)

Spot number and description[a]		Common 206Pb (%)[b]	U (ppm)	Th (ppm)	Th/U	^{207}Pb corrected		Uncorrected ratios		^{204}Pb corrected ratios	
						^{206}Pb/^{238}U age	^{206}Pb*/^{238}Uc	^{238}U/^{206}Pb	^{207}Pb/^{206}Pb	^{238}U/^{206}Pb*c	^{207}Pb*/^{206}Pb*c
A Silva 2: Metagranodiorite. UTM: 538749, 4775197, 354											
21	o	0.05	223	69	0.32	486.0 ± 1.4	0.0783 ± 0.0005	12.76 ± 0.6	0.0573 ± 1.7	12.76 ± 0.6	0.0576 ± 1.7
22	o	0.02	560	53	0.10	523.7 ± 1.0	0.0846 ± 0.0003	11.81 ± 0.4	0.0580 ± 1.1	11.82 ± 0.4	0.0579 ± 1.1
23	o	−0.01	592	65	0.11	532.6 ± 1.0	0.0861 ± 0.0003	11.61 ± 0.4	0.0580 ± 1.0	11.62 ± 0.4	0.0575 ± 1.2
24	o	0.76	771	96	0.13	508.6 ± 0.9	0.0821 ± 0.0003	12.09 ± 0.3	0.0636 ± 2.2	12.17 ± 0.4	0.0583 ± 3.0
25	o	0.10	321	26	0.08	498.7 ± 1.2	0.0804 ± 0.0004	12.42 ± 0.5	0.0580 ± 1.4	12.42 ± 0.5	0.0579 ± 1.4
26.1	r	−0.04	599	29	0.05	517.3 ± 0.9	0.0835 ± 0.0003	11.97 ± 0.4	0.0573 ± 1.0	11.98 ± 0.4	0.0571 ± 1.0
26.2	r	−0.16	575	92	0.17	525.3 ± 1.1	0.0849 ± 0.0004	11.80 ± 0.4	0.0566 ± 1.1	11.80 ± 0.4	0.0567 ± 1.1
27	o	0.05	894	46	0.05	505.3 ± 0.8	0.0815 ± 0.0003	12.26 ± 0.3	0.0577 ± 0.9	12.26 ± 0.3	0.0577 ± 0.9
28	o	0.03	359	40	0.12	515.1 ± 1.2	0.0832 ± 0.0004	12.02 ± 0.5	0.0579 ± 1.3	12.03 ± 0.5	0.0572 ± 1.4
29	o	0.00	308	101	0.34	506.2 ± 1.2	0.0817 ± 0.0004	12.24 ± 0.5	0.0574 ± 1.4	12.24 ± 0.5	0.0576 ± 1.4
30	o	−0.04	375	53	0.15	504.1 ± 1.1	0.0813 ± 0.0004	12.30 ± 0.5	0.0570 ± 1.3	12.31 ± 0.5	0.0565 ± 1.4
31	o	1.24	655	50	0.08	506.4 ± 0.9	0.0817 ± 0.0003	12.09 ± 0.3	0.0675 ± 0.9	12.27 ± 0.4	0.0552 ± 2.7
32	o	−0.02	238	38	0.16	499.2 ± 1.4	0.0805 ± 0.0005	12.42 ± 0.6	0.0571 ± 1.6	12.43 ± 0.6	0.0564 ± 1.8
33	o	0.20	195	27	0.14	508.9 ± 1.6	0.0821 ± 0.0006	12.15 ± 0.6	0.0591 ± 1.8	12.17 ± 0.7	0.0577 ± 2.1
34	o	0.03	388	37	0.10	498.6 ± 1.1	0.0804 ± 0.0004	12.43 ± 0.4	0.0575 ± 1.2	12.43 ± 0.4	0.0574 ± 1.2
35	o	−0.04	461	54	0.12	522.4 ± 1.1	0.0844 ± 0.0004	11.85 ± 0.4	0.0575 ± 1.2	11.85 ± 0.4	0.0576 ± 1.2

All errors are 1s.

[a] Zircon characterization: o = oscillatory zoning; c = core; r = rim; inher = inheritance; hcPb = high common Pb.

[b] Negative values denote reversely discordant analyses.

[c] Pb* denotes radiogenic lead.

According to Wooden et al. (2006), for common magmatic suites the Yb/Gd ratio, which represents the steepness of the HREE pattern, shows a starting ratio of about 10 and it increases rapidly at relatively low temperatures (<750 °C). This increase in the steepness can be related to the fractionation of middle (M) REE from the melt during the crystallization of accessory minerals (mainly apatite and titanite). In contrast, Th/U tends to decrease with decreasing zircon crystallization temperature, showing the strongest change at higher T. Hafnium concentration in zircon is usually higher as fractional crystallization progresses and temperature decreases.

Additionally, the Ce/Sm ratio typically rises with increasing fractionation (e.g., Yb/Gd ratio). Ce/Sm is preferred as a monitor of magma evolution rather than Ce/Ce* because it varies more regularly when plotted against a fractionation index (Wooden et al., 2006).

We have plotted these ratios for the A Silva magmatic zircons, together with those of zircon standard R33 analyzed in the same sessions for comparison. In a Th/U versus Yb/Gd plot (Fig. 7a), R33 (diamonds) shows a reversely correlated asymptotic trend, which is typical of a suite of zircons that have crystallized in an evolving magma (Wooden et al., 2006); i.e., zircon chemistry reflects the degree of its host rock fractionation (Belousova et al., 2002). Contrastingly, Yb/Gd ratio for the A Silva zircons shows a limited variation from 10 to 20 and most of the A Silva zircons have low Th/U, ranging from 0.04 to 0.3, even though there is some scatter in the Th/U ratio (seven analyses between 0.3 and 0.6). The A Silva zircons have significantly low and constant Ce to Sm ratios compared to those of the zircon standard (Fig. 7b). The homogeneity in the fractionation indices has important implications for the age assessment, as it precludes the possibility of a dominant zircon inherited component or the process of fractional crystallization in a long-lived magmatic chamber (see discussion in Section 5.2).

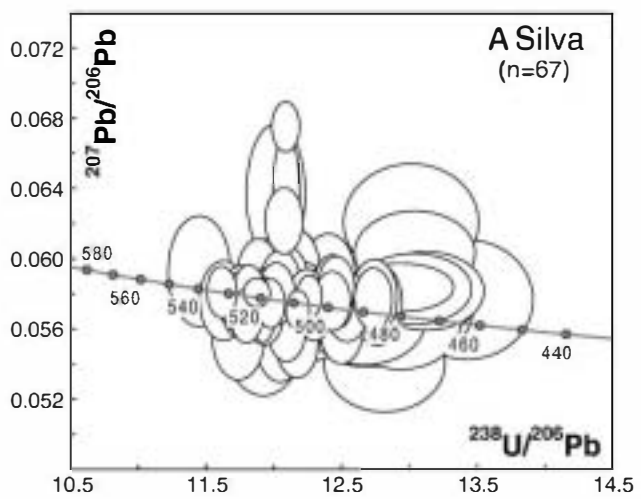

Fig. 4. Tera-Wasserburg plot showing distribution of SHRIMP zircon analyses from the A Silva samples. Error ellipses are ±2σ.

Further petrogenetic information can be suggested using other elemental ratios. It is observed that, in general terms, metamorphic zircon has higher U concentration than magmatic ones, whereas Ce is higher in magmatic zircon (e.g., Hoskin and Schaltegger, 2003). Using a vast zircon geochemistry dataset obtained from a variety of geological samples, the scientific staff from SUMAC devised a bilogarithmic plot of the U/Ce ratio versus Th concentration in which a 1:1 line separates magmatic from metamorphic zircons. This plot is shown in Fig. 7c for the R33 standard and the A Silva zircon data. Noticeably, R33 plots in the magmatic field conforming to a linear trend with positive slope, whereas the A Silva zircons plot in the metamorphic field, in agreement with the anatectic character of the granodiorite.

On a Hf versus Eu/Eu* plot (Fig. 7d), the depth of the Eu anomaly in the A Silva zircons stands out compared to the anomaly of the zircon standard, and is interpreted to be the consequence of coeval plagioclase growth which strongly fractionated Eu^{+2} from the melt.

5.2. Crystallization age of the A Silva Granodiorite

The smooth variation in age observed in the A Silva zircons (from 530 to 460 Ma) can be interpreted in three different ways: (1) It reflects analytical scatter; (2) it is a true difference in age; or (3) it is the result of some combination of Pb-loss and inheritance (Coleman et al., 2004; McClelland et al., 2006). The first explanation, analytical scatter, cannot be invoked to account for the 70 m.y. range in age of the A Silva zircon, because the age range is similar in both samples regardless of the analytical session, and there is no correlation between U concentration and age. The second alternative requires either a long-lived magmatic chamber (although 70 m.y. is an unreasonable time span) or a sequence of different geological processes in a short time span, such as metamorphism and magmatism. However, the homogeneity in the zircon fractionation indices, such as Yb/Gd, Th/U and Hf, suggests that zircon from the A Silva granodiorite grew during a single igneous event

Table 2
Rare earth element (REE) and Hf data for zircons from the A Silva granodiorite.

Spot number and description[a]		U	Th	Hf	La	Ce	Nd	Sm	Eu	Gd	Dy	Er	Yb	Lu	Y	Th/U	Yb/Gd	Eu/Eu*	Ce/Sm	U/Ce
A Silva-1 (first aliquot)																				
1		390	51	12,311	0.033	1.65	1.08	4.98	0.15	69	431	862	1469	n.a.	n.a.	0.13	21.2	0.02	0.33	236
2		234	130	9349	0.435	5.16	4.20	9.88	0.56	89	328	535	837	n.a.	n.a.	0.55	9.4	0.06	0.52	45
3		187	35	11,586	0.030	1.39	0.96	3.47	0.12	43	195	309	469	n.a.	n.a.	0.19	11.0	0.03	0.40	134
4		1566	81	14,989	0.201	1.48	0.81	3.60	0.14	59	429	720	1252	n.a.	n.a.	0.05	21.2	0.03	0.41	1057
5		226	48	12,077	0.026	1.36	0.92	4.00	0.13	50	193	270	391	n.a.	n.a.	0.21	7.8	0.03	0.34	167
6		170	32	10,882	0.015	1.34	0.85	3.40	0.14	42	193	300	455	n.a.	n.a.	0.19	10.8	0.04	0.39	127
7		336	40	12,316	0.053	4.10	0.28	1.36	0.11	21	119	169	249	n.a.	n.a.	0.12	12.1	0.07	3.02	82
8		742	149	11,503	0.478	3.39	1.52	5.91	0.19	81	445	709	1027	n.a.	n.a.	0.20	12.8	0.03	0.57	219
9		196	36	11,011	0.021	1.51	1.17	4.72	0.12	61	330	634	1035	n.a.	n.a.	0.18	16.9	0.02	0.32	130
10		211	35	10,959	0.021	1.38	1.02	4.52	0.11	59	331	623	1044	n.a.	n.a.	0.16	17.7	0.02	0.30	153
11		235	59	10,183	0.331	2.29	2.00	5.86	0.18	70	311	533	814	n.a.	n.a.	0.25	11.7	0.03	0.39	103
12		166	18	11,397	0.006	0.72	0.44	2.34	0.09	35	182	256	331	n.a.	n.a.	0.11	9.4	0.03	0.31	231
13		143	53	9949	0.149	2.59	2.81	7.82	0.26	79	315	537	856	n.a.	n.a.	0.37	10.9	0.03	0.33	55
14		164	69	10,049	0.032	2.43	2.64	7.67	0.17	78	287	475	751	n.a.	n.a.	0.42	9.6	0.02	0.32	68
15		291	34	11,883	0.016	1.14	0.72	3.44	0.10	49	306	590	995	n.a.	n.a.	0.12	20.4	0.02	0.33	254
16		217	42	11,107	0.019	1.42	1.06	4.39	0.15	58	260	390	543	n.a.	n.a.	0.19	9.4	0.03	0.32	153
17		130	62	10,590	0.019	3.16	1.36	4.70	0.19	53	211	375	612	n.a.	n.a.	0.48	11.6	0.04	0.67	41
A Silva-1 (second aliquot)																				
1.1	OR-YC	130	72	10,573	0.024	n.a.	2.75	7.75	0.20	77	285	477	771	140	2756	0.55	10.1	0.03	–	–
1.2	OR-YC	401	70	12,781	8.660	n.a.	5.91	6.82	0.46	63	283	379	535	87	2829	0.18	8.5	0.07	–	–
2.1	OR-YC	654	72	12,701	0.006	n.a.	0.79	3.55	0.11	54	301	471	714	118	3155	0.11	13.3	0.03	–	–
2.2	OR-YC	148	57	10,763	0.017	n.a.	2.03	6.04	0.18	63	227	374	589	103	2276	0.39	9.4	0.03	–	–
3.1	OR-YC	554	97	13,040	1.067	n.a.	1.58	5.19	0.23	69	404	650	992	163	4090	0.17	14.3	0.04	–	–
3.2	OR-YC	115	44	11,057	0.026	n.a.	1.41	4.12	0.11	45	181	321	529	95	1795	0.38	11.8	0.02	–	–
4		483	58	13,184	0.135	n.a.	1.11	4.92	0.09	64	372	703	1285	227	4055	0.12	20.0	0.02	–	–
5.1	OR-YC, Inher II	617	50	13,635	1.686	n.a.	1.49	4.24	0.21	55	319	438	573	88	3283	0.08	10.4	0.04	–	–
5.2	OR-YC	226	53	12,179	0.015	n.a.	1.99	7.11	0.24	90	444	816	1312	228	4730	0.24	14.6	0.03	–	–
6		351	45	14,076	0.009	n.a.	0.71	2.61	0.11	38	214	362	573	99	2393	0.13	14.9	0.03	–	–
7.1	Inher II	491	460	11,044	0.063	n.a.	5.93	14.57	0.59	115	390	623	938	159	3707	0.94	8.1	0.04	–	–
7.2		598	56	12,791	0.710	n.a.	1.61	4.43	0.22	58	329	454	605	94	3474	0.09	10.5	0.04	–	–
8.1	OR-YC	381	47	12,978	0.273	n.a.	4.58	10.96	0.31	123	639	1212	2027	346	6968	0.12	16.5	0.03	–	–
8.2	OR-YC	1152	87	14,174	0.066	n.a.	0.69	3.65	0.12	60	406	666	1050	172	4244	0.08	17.6	0.03	–	–
9	Inher II	263	66	11,786	1.190	n.a.	3.03	8.82	0.31	100	429	725	1158	197	4296	0.25	11.6	0.03	–	–
10	Inher II	414	167	11,372	3.372	n.a.	6.42	10.30	0.33	101	461	798	1277	216	4657	0.40	12.6	0.03	–	–
11	Inher II	134	69	9801	0.023	n.a.	3.08	7.33	0.93	70	259	434	693	121	2496	0.51	9.9	0.13	–	–
12	Inher II	344	235	9725	0.105	n.a.	11.78	27.90	1.03	253	1047	1597	2227	357	9565	0.68	8.8	0.04	–	–
13.1	OR-YC	67	24	10,304	0.018	n.a.	1.23	3.67	0.25	41	191	349	577	101	1994	0.35	14.1	0.06	–	–
13.2	OR-YC	401	54	11,592	0.099	n.a.	1.90	6.63	0.20	79	361	494	697	114	3564	0.14	8.8	0.03	–	–
14	Inher II	295	133	11,523	0.043	n.a.	5.36	14.07	0.37	135	465	690	1030	179	4215	0.45	7.6	0.03	–	–
15.1	OR-YC	135	34	11,479	0.017	n.a.	1.59	5.80	0.23	67	263	272	261	37	2182	0.25	3.9	0.04	–	–
15.2	OR-YC	582	42	12,682	0.009	n.a.	0.59	2.96	0.11	40	259	437	735	124	2728	0.07	18.2	0.03	–	–
16.1		759	37	14,474	0.008	n.a.	0.38	2.29	0.06	42	320	534	840	132	3613	0.05	20.1	0.02	–	–
16.2	Inher I	85	40	9622	0.008	n.a.	0.58	1.24	0.71	10	31	64	160	37	387	0.47	16.6	0.63	–	–
17		687	74	12,758	0.013	n.a.	0.98	5.00	0.11	69	372	601	937	154	3829	0.11	13.6	0.02	–	–
18		295	47	12,853	0.793	n.a.	1.80	3.86	0.20	50	256	371	523	86	2441	0.16	10.5	0.04	–	–
19		614	37	13,680	0.052	n.a.	0.50	2.62	0.09	40	248	356	512	81	2518	0.06	12.7	0.03	–	–
20		433	26	13,644	0.004	n.a.	0.28	1.84	0.06	29	199	312	443	70	2109	0.06	15.5	0.02	–	–
21		333	60	11,940	0.008	n.a.	1.49	6.17	0.18	82	441	756	1200	204	4461	0.18	14.6	0.02	–	–
A Silva-2																				
1		243	41	13,179	0.440	2.30	1.50	3.88	0.18	46	210	301	446	73	1922	0.17	9.8	0.04	0.59	106
2		337	53	12,363	0.019	2.13	2.87	10.00	0.43	109	376	314	290	39	2925	0.16	2.7	0.04	0.21	159
3		244	63	11,640	0.545	3.02	2.34	7.50	0.25	79	331	533	830	142	3282	0.26	10.6	0.03	0.40	81
4		654	83	13,553	0.104	1.84	1.35	5.93	0.22	83	501	856	1442	238	5356	0.13	17.4	0.03	0.31	355
5	HcPb	962	79	14,884	15.400	50.58	28.30	26.08	3.59	132	625	828	1266	200	5195	0.08	9.6	0.19	1.95	19
6		377	50	12,637	0.016	1.33	0.94	4.06	0.12	55	291	476	746	124	2906	0.13	13.5	0.02	0.33	284
7		388	28	13,021	0.422	1.36	0.54	2.53	0.09	40	282	505	778	124	3128	0.07	19.6	0.03	0.54	286
8		334	20	13,293	0.009	0.57	0.31	1.61	0.05	26	167	242	340	53	1747	0.06	13.2	0.03	0.35	591
9		358	39	12,570	0.108	1.17	0.96	4.61	0.14	59	288	396	541	86	2764	0.11	9.1	0.03	0.25	305
10		1536	55	17,130	0.639	2.48	1.28	3.93	0.21	53	387	586	911	140	4041	0.04	17.2	0.04	0.63	620
11		383	30	13,051	0.003	0.82	0.62	2.94	0.10	42	224	303	403	63	2295	0.08	9.7	0.03	0.28	464
12		323	66	12,128	0.019	1.74	1.55	5.85	0.12	65	304	455	675	111	2920	0.20	10.4	0.02	0.30	186
13		177	46	11,651	0.019	2.19	2.27	6.39	0.31	64	282	495	784	136	2929	0.26	12.2	0.05	0.34	81
14		880	46	14,078	0.009	0.79	0.57	3.27	0.09	51	348	493	650	90	3477	0.05	12.9	0.02	0.24	1110
15		320	53	11,946	0.443	2.90	1.44	4.08	0.21	50	270	433	653	107	2660	0.16	13.0	0.05	0.71	111
16		331	43	12,204	0.035	1.37	1.30	5.71	0.21	72	374	587	882	147	3687	0.13	12.3	0.03	0.24	241
17		298	24	12,689	0.008	0.65	0.40	2.34	0.08	35	196	290	421	69	1963	0.08	11.9	0.03	0.28	457
18		273	41	11,899	0.010	1.35	1.20	4.64	0.16	61	319	572	930	161	3270	0.15	15.2	0.03	0.29	202
19		343	34	12,370	0.008	1.01	0.84	4.20	0.14	61	342	548	810	132	3575	0.10	13.2	0.03	0.24	339
20		551	44	13,079	0.006	0.87	0.54	3.00	0.09	46	301	443	595	89	3065	0.08	12.8	0.02	0.29	630
21		222	68	10,810	0.030	2.64	2.69	8.46	0.21	89	380	651	1038	180	3788	0.31	11.7	0.02	0.31	84

(continued on next page)

Table 2 (*continued*)

Spot number and description[a]	U	Th	Hf	La	Ce	Nd	Sm	Eu	Gd	Dy	Er	Yb	Lu	Y	Th/U	Yb/Gd	Eu/Eu*	Ce/Sm	U/Ce
A Silva-2																			
22	544	50	12,980	1.594	2.84	1.12	2.89	0.09	42	270	409	572	89	2915	0.09	13.7	0.02	0.98	191
23	577	63	11,859	0.161	1.63	1.95	5.73	0.17	71	372	554	814	132	3812	0.11	11.5	0.02	0.28	354
24	772	95	13,821	1.622	5.68	3.04	6.58	0.49	70	401	631	933	145	3927	0.12	13.3	0.07	0.86	136
25	319	25	13,196	0.008	0.86	0.78	3.55	0.17	44	165	150	167	25	1292	0.08	3.8	0.04	0.24	369
26.1	603	29	13,645	0.007	0.63	0.24	1.72	0.05	29	233	364	485	69	2554	0.05	16.5	0.02	0.37	949
26.2	576	91	12,694	0.047	2.40	3.22	11.77	0.23	145	818	1508	2462	401	8796	0.16	17.0	0.02	0.20	240
27	908	45	14,994	0.109	1.00	0.45	2.78	0.08	45	348	536	740	107	3651	0.05	16.6	0.02	0.36	910
28	357	39	12,656	0.014	1.13	0.98	4.63	0.15	64	373	622	947	156	3776	0.11	14.8	0.03	0.24	315
29	306	99	11,662	0.028	2.80	2.27	6.57	0.25	72	351	622	977	166	3576	0.32	13.7	0.04	0.43	109
30	372	52	11,778	0.015	1.47	1.30	4.84	0.15	63	334	565	879	147	3463	0.14	13.9	0.03	0.30	252
31	654	49	13,086	0.476	1.85	0.99	4.08	0.15	58	372	518	683	101	3633	0.08	11.8	0.03	0.45	354
32	239	37	11,444	0.025	1.42	1.10	4.32	0.14	56	299	536	855	146	3086	0.16	15.2	0.03	0.33	168
33	189	26	12,360	0.012	1.14	0.71	2.94	0.12	40	240	470	807	142	2698	0.14	20.3	0.03	0.39	166
34	393	37	12,408	0.005	1.02	0.84	4.10	0.10	56	347	606	1014	171	3575	0.09	18.3	0.02	0.25	386
35	453	53	12,177	0.010	1.62	1.30	5.74	0.20	77	393	584	826	135	3502	0.12	10.7	0.03	0.28	280

[a] Zircon description. OR-YC, old rim-young core; Inher I, inherited age; Inher II, spot interpreted as inherited (see Fig. 5); HcPb, high common Pb; n.a., not analyzed.

with limited fractional crystallization, hence precluding the possibility that the age range represents a true variation in age.

The last option to explain the age dispersion involves a combination of Pb-loss and inheritance. As shown in Section 2, the A Silva granodiorite is generated from the melting of the O Pino metasediments, which has detrital zircons (Abati et al., 2007) that record an almost continuous age distribution of magmatism (from 640 to 510 Ma) and metamorphism (from 510 to 480 Ma). Even though we selected the cleanest and longest zircon grains during the final hand picking in order to avoid inherited zircons, it is impossible to distinguish detrital grains that have experienced very little abrasion from those generated during the A Silva granodiorite crystallization on the basis of morphology alone. However, excluding the oldest grains with higher Th/U ratios, the homogeneity in the zircon fractionation indices suggests that the inherited component involved in the analyzed A Silva zircon population is negligible.

Thus, the most probable process controlling the wide age distribution is Pb-loss. Accordingly, we used the TuffZirc method, developed by Ludwig and Mundil (2002), to obtain a reliable age from a dataset affected by slightly positive and negative age biases. The best age estimate obtained is 510.28 (+1.57, −1.44)Ma (Fig. 8), using the TuffZirc algorithm on a group of 60 analyses ranging from 530 to 460 Ma. This age is the median obtained by pooling together eleven analyses, considering the largest set of internally concordant dates that are statistically coherent, and it is interpreted as the best statistical estimate for the crystallization age of the A Silva granodiorite. Ages calculated using this method are reliable provided the eleven selected analyses are cogenetic and unaffected by Pb-loss. In this case, we can argue the validity of these assumptions based on the zircon CL features

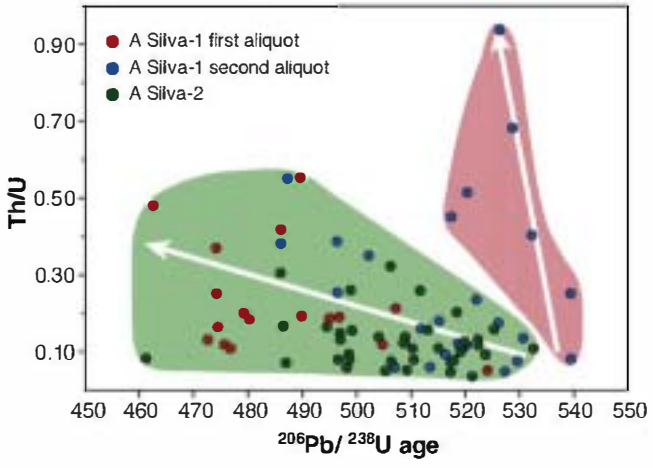

Fig. 5. Th/U versus $^{206}Pb/^{238}U$ age for the analyzed A Silva zircons. See Section 4.3 for explanation.

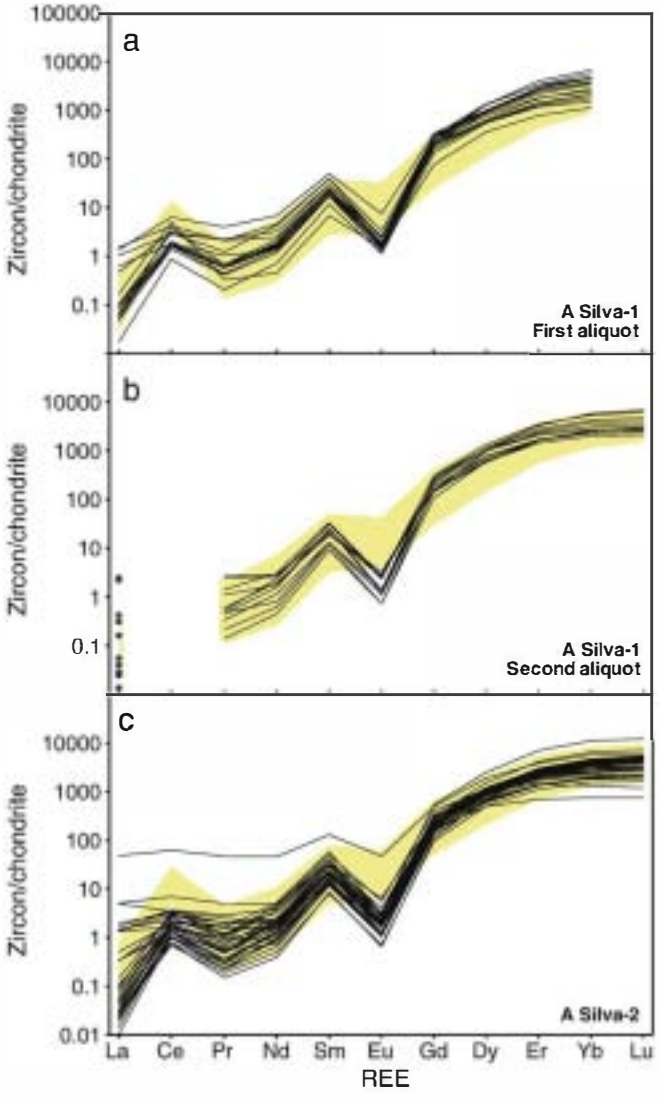

Fig. 6. Chondrite-normalized rare earth element (REE) patterns for (a) 17 analyses from the A Silva-1 first session, (b) 30 analyses of the A Silva-1 second session, and (c) 36 analyses of the A Silva-2 sample. Light yellow fields represent the REE patterns for the standard R33, included for comparison.

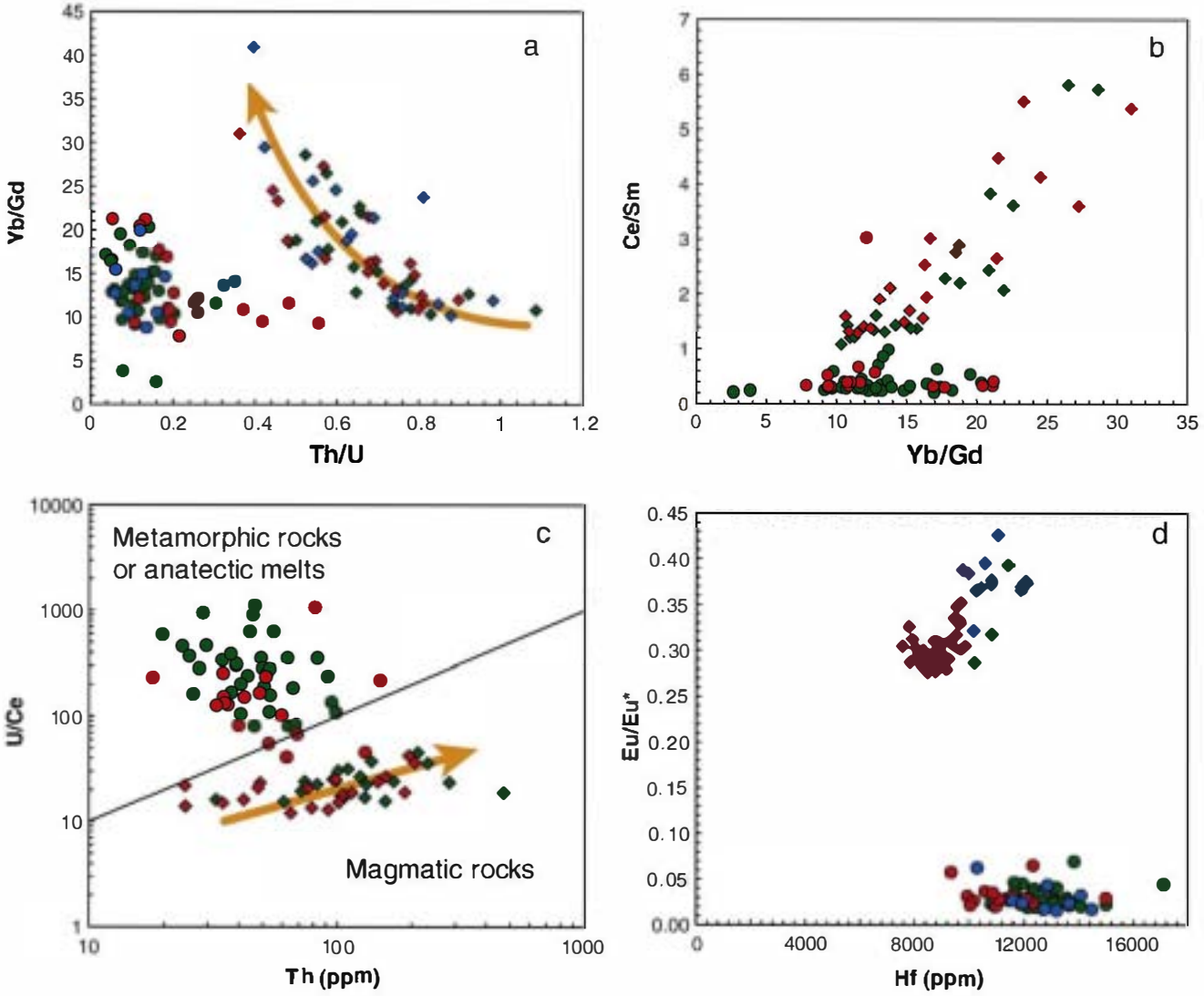

Fig. 7. (a) Th/U versus Yb/Gd plot. (b) Ce/Sm versus Yb/Gd plot. (c) Th versus U/Ce plot. (d) Hfversus Eu/Eu* plot. See Section 4.4 for explanation.

and geochemistry, i.e. oscillatory zoning consistent with zircons grown in igneous rocks (Corfu et al., 2003) and homogeneous fractionation indices.

5.3. Constraints on the evolution of the Upper units

The new U–Pb zircon age supplied by the A Silva granodiorite (510 Ma) indicates that it is an old plutonic body enclosed within the widespread Cambrian–Ordovician magmatism (520–495 Ma). This magmatism has been widely documented in the upper units of the allochthonous complexes (van Calsteren et al., 1979; Peucat et al., 1990; Schäfer et al., 1993; Abati et al., 1999; 2007; Santos Zalduegui et al., 2002) and in other areas of the northern Gondwana margin (see Murphy et al., 2010, and references therein). In addition, the preservation of the original relationships with the upper unit host rocks in its western and upper contacts makes this plutonic body a suitable place to examine key aspects of the Cambrian–Ordovician pre-orogenic evolution of the continental margin of Gondwana. The upper units represent different crustal levels of the arc crust at that time and record processes such as granite emplacement, regional extension and exhumation of the HP–HT rocks situated below.

Field relationships suggest that the A Silva granodiorite was emplaced after crustal thickening in the IP unit, which metamorphic peak conditions for the IP units are estimated at 10 kb and 650 °C in the O Pino schists (Castiñeiras, 2005). Subsequent decompression *P–T* conditions have been estimated at 4 kb and *T*>650 °C in the HP–HT units (Gómez Barreiro, 2007).

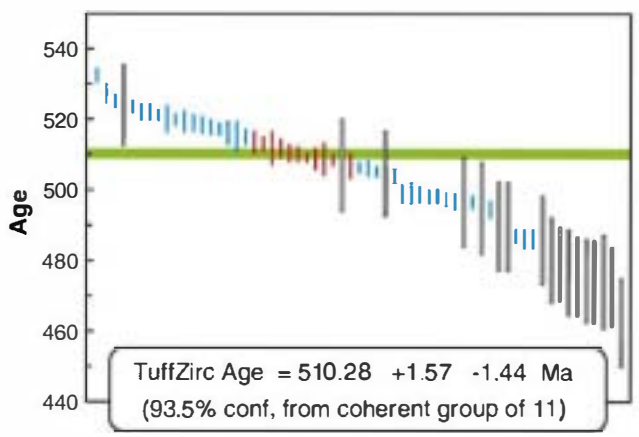

Fig. 8. Age distribution for the 61 magmatic zircons analyzed. White bars, analyses not considered in the TuffZirc calculation; blue bars, rejected analyses; red bars, analyses used to obtain the best age estimate. See Section 5.2 for explanation.

The laccolithic/sill-like geometries shown by the A Silva granodiorite are likely to be the result of their intrusion within a generalized, subhorizontal, kilometre-thick, shear zone with top-to-the-NNW kinematics, where positive feedback between melting and shearing may occur. This scenario promotes subhorizontal host rock displacements, magma accumulation, magmatic wedging and stopping, thus giving rise during progressive deformation to multiple intrusions as has been documented in several cases (e.g., Brown and Solar, 1998).

In a more regional context, the emplacement of the A Silva granodiorite and its diatexite envelope was followed by the intrusion of a number of gabbroic rocks (Monte Castelo gabbro) and small plutons in the metatexitic country rocks that escaped to the main regional deformation suggesting that this extensional episode occurred at 510 to 495 Ma.

In addition, the intrusion of diabasic dikes that cross cut the regional S2 foliation in the uppermost unit yield a U–Pb age of 510 Ma (Díaz García et al., 2010), supporting the aforementioned minimum age for the extensional shearing in the IP–IHT upper units.

The plutonic complex formed by the A Silva granodiorite, the Monte Castelo gabbro and minor intrusive bodies was determined in the top-to-the-NNW shear zone, giving rise to the piling of the plutonic sheets, reaching at least the present thickness of 8 km within an antiformal stack. This thickening event, could by itself be responsible for the near isothermal pressure increase to the granulite facies (from 6 to 8 kb) that has been recorded exclusively in the basal shear zones of this antiformal stack affecting the Monte Castelo gabbro (Abati et al., 2003). The timing of this localized compressional event was from 495 to 480 Ma (Abati et al., 2003; 2007).

These compressional structures and the related pressure increase have not been identified in the remaining units, and probably reflect a transitory stage of thickened middle crust that occurred after the cooling and crystallization of the gabbroic to granodioritic complex, promoting vertical decoupling within this orogenic lithosphere.

In contrast, in the HP–HT upper units, this compressional event has not been recognized, but the available data demonstrate that eclogite and granulite rocks underwent intense ductile deformation, accompanied by partial melting and followed by widespread development of an amphibolite facies foliation related to their continued exhumation (e.g., Ábalos, 1997; Gómez Barreiro et al., 2006).

Later structures consist of more localized extensional detachments (BD, XD, CD and FD in Figs. 1 and 2) developed in kinematic continuity with the top-to-the-NNW shearing that affect all the upper units and eventually brought together the uppermost and HP–HT units, completing the thinning of the upper units. Hornblende from mylonitic fabrics related to the Fornás detachment (FD) yielded exhumation ages for the HP–HT units of around 420 Ma (Gómez Barreiro et al., 2006), in agreement with other amphibolite facies retrogressed-foliation ages in HP–HT upper units (425 Ma, Dallmeyer et al., 1997). According to these dates, the HP–HT upper units underwent an unroofing event in the footwall of an extensional shear zone with roughly top-to-the-north kinematics during a protracted time span, indicating a large residence time under lower and middle crustal conditions. This situation could satisfactorily explain the scattered ages from 495 to 430 Ma in the zircons extracted from leucosomes (Peucat et al., 1990; Fernández Suárez et al., 2003, 2007), and independently support the idea that peak metamorphic conditions for the HP–HT units would date back to 510 Ma.

The geodynamic framework proposed by several authors for the northern part of Gondwana, similar to other large and hot orogens, enables us to situate these processes of melting at the mid-crustal levels, followed by magmatic underplating, extension, and exhumation of the HP–HT rocks (Murphy et al., 2006; Gómez Barreiro et al., 2007; Linnemann et al., 2008; Martínez Catalán et al., 2009). These authors have suggested a geodynamic model that occurs diachronously along the northern Gondwana margin and consists of a Late Neoproterozoic to Early Cambrian ridge–trench collision, leading to the termination of subduction and the generation of a continental transform during the Cambrian. This event was followed by the individualization of a continental ribbon that drifted away from Gondwana as the intervening Rheic Ocean expanded. According to Fuenlabrada et al. (2010), and Díaz García et al. (2010), the accretionary processes, recorded by the earliest structures developed in the low-grade part of the upper unit, would have continued until 510 Ma. This age, provided by post- to syn-tectonic mafic dikes, marks the change to a period of north-directed extension, anatexis, intrusion of arc plutonics, and mafic dyking, probably linked to ridge subduction and a change to an extensional regime that leads to strong thinning of the arc crust and the exhumation of the arc-root which culminates in the opening of the Rheic Ocean.

6. Conclusions

This study provides significant insight into the A Silva granodiorite and increases its value as a marker within the tectonic evolution of the intermediate-pressure unit of the Allochthonous complexes of the Iberian massif.

The results from eighty-three analyses performed in 73 zircon grains from two samples define a near-concordant age range between 540 and 460 Ma. Taking into account a coupled assessment with the REE and Hf composition of the zircons, we obtained a $^{206}Pb/^{238}U$ crystallization age of 510.28 (+1.57, −1.44)Ma using the TuffZirc algorithm, designed to obtain an age from a dataset affected by Pb-loss or slight inheritance,.

The A Silva granodiorite consists of multiple sheets intruded in a sequence of metatexitic host rocks after an early stage of crustal thickening (up to 10 kb) and during subsequent decompression (ca. 4 kb) that developed coevally with partial melting in the final stages of the D2 regional extensional event.

Subsequent to its cooling and crystallization, the whole gabbroic and granodioritic complex underwent a transitory compressional stage within a generalized extensional scenario. The complex was affected by top-to-the-NNW shearing, thus developing a flat-lying S–C type foliation and forming an antiformal stack structure in a N–S profile. The basal shear zones of this 8 km-thick duplex registered a 2–4 kb pressure increase between 495 to 480 Ma.

Field relationships with the country rocks allow us to deduce that crustal thickening and the earliest stages of subsequent extension was completed by Upper Cambrian time in the intermediate-pressure upper units of the Allochthonous complexes.

Acknowledgements

We would like to dedicate this work to the memory of our beloved colleague and friend Florentino Díaz García, who sadly passed away last August.

Pablo González Cuadra is kindly thanked for his assistance during the sampling. Joe Wooden and the SUMAC staff at Stanford University are especially acknowledged for their help in operating the SHRIMP instrument and in interpreting the results. J. Abati and R. Arenas are also thanked for their constructive comments of an early version of the manuscript. The original manuscript has greatly benefited from insightful reviews by B. Murphy, J. Wooden and W. Premo.

Financial support for this research has been provided by Spanish project CGL2007-65338-CO2/BTE (Ministerio de Ciencia e Innovación). This study is also a contribution to the IGCP-497 project: "The Rheic Ocean: Origin, evolution and correlatives". P. Castiñeiras's stay at the SUMAC facility was financed with a "Profesores UCM en el extranjero" travel aid. J. Gómez Barreiro was supported by a MEC-Juan de la Cierva Postdoctoral contract.

References

Ábalos, B., 1997. Omphacite fabric variation in the Cabo Ortegal eclogite (NW Spain): relationships with strain symmetry during high-pressure deformation. Journal of Structural Geology 19 (5), 621–631.

Abati, J., Arenas, R., Martínez Catalán, J.R., Díaz García, F., 2003. Anticlockwise P–T path of granulites from the Monte Castelo Gabbro (Órdenes Complex, NW Spain). Journal of Petrology 44 (2), 305–327.

Abati, J., Castiñeiras, P., Arenas, R., Fernández Suárez, J., Gómez-Barreiro, J., Wooden, J., 2007. Using SHRIMP zircon dating to unravel tectonothermal events in arc environments. The early Palaeozoic arc of NW Iberia revisited, 19. Terra Nova, pp. 432–439.

Abati, J., Dunning, G.R., Arenas, R., Díaz García, F., González Cuadra, P., Martínez Catalán, J.R., Andonaegui, P., 1999. Early Ordovician orogenic event in Galicia (NW Spain): evidences from U–Pb ages in the uppermost unit of the Órdenes Complex. Earth and Planetary Science Letters 165, 213–228.

Anders, E., Grevesse, N., 1989. Abundances of the elements: meteoritic and solar. Geochimica et Cosmochimica Acta 53, 197–204.

Andonaegui, P., González Cuadra, P., Castiñeiras, P., Martínez Catalán, J.R., Arenas, R., Díaz García, F., Abati, J., Sánchez Martínez, S., 2007. Geochronology and geochemistry of the Corredoiras orthogneiss (Ordenes complex, Iberian Massif, NW Spain. In: Arenas, R., Martínez Catalán, J.R., Abati, J., Sánchez Martínez, S. (Eds.), The Rootless Variscan Suture of NW Iberia (Galicia, Spain). Field Trip and Conference Abstracts IGME, 188.

Andonaegui, P., Gonzálezdel Tánago, J., Arenas, R., Abati, J., Martínez Catalán, J.R., Peinado, M., Díaz García, F., 2002. Tectonic setting of the Monte Castelo gabbro (Ordenes Complex, northwestern Iberian Massif): Evidence for an arc-related terrane in the hanging wall to the Variscan suture. In: Martínez Catalán, J.R., Hatcher Jr., R.D., Arenas, R., Díaz García, F. (Eds.), Variscan–Appalachian Dynamics: the Building of the Late Paleozoic Basement: Geological Society of America Special Paper, 364, pp. 37–56.

Arenas, R., Martínez Catalán, J.R., 2002. Prograde development of corona textures in metagabbros of the Sobrado window (Ordenes Complex, NW Iberian Massif). In: Martínez Catalán, J.R., Hatcher Jr., R.D., Arenas, R., Díaz García, F. (Eds.), Variscan–Appalachian Dynamics: the Building of the Late Paleozoic Basement: Geological Society of America Special Paper, 364, pp. 73–88.

Arenas, R., Rubio Pascual, F.J., Díaz García, F., Martínez Catalán, J.R., 1995. High-pressure microinclusions and development of an inverted metamorphic gradient in the Santiago Schists (Órdenes Complex, NW Iberian Massif, Spain): evidence of subduction and syn-collisional decompression. Journal of Metamorphic Geology 13, 141–164.

Bellido, F., González Lodeiro, F., Klein, E., Martínez Catalán, J.R., Pablo Macia, J.G., 1987. Las rocas graníticas hercínicas del Norte de Galicia y Occidente de Asturias. Memorias del Instituto Geológico y Minero de España 101, 157.

Belousova, E.A., Griffin, W.L., O'Reilly, S.Y., Fisher, N.I., 2002. Igneous zircon: trace element composition as an indicator of source rock type. Contributions to Mineralogy and Petrology 143, 602–622.

Black, L.P., Kamo, S.L., Allen, C.M., Davis, D.W., Aleinikoff, J.N., Valley, J.W., Mundil, R., Campbell, I.H., Korsch, R.J., Williams, I.S., Foudoulis, C., 2004. Improved $^{206}Pb/^{238}U$ microprobe geochronology by the monitoring of a trace-element-related matrix effect, SHRIMP, ID-TIMS, ELA-ICP-MS and oxygen isotope documentation for a series of zircon standards. Chemical Geology 205, 115–140.

Bozkurt, E., Pereira, M.F., Strachan, R.A., Quesada, C., 2008. Evolution of the Rheic Ocean. Tectonophysics 461, 1–8.

Brown, M., Solar, G.S., 1998. Shear-zone systems and melts: feedback relations and self-organization in orogenic belts. Journal of Structural Geology 20 (213), 211–227.

Butera, K.M., Williams, I.S., Blevin, P.L., Simpson, C.J., 2001. Zircon U–Pb dating of Early Paleozoic monzonitic intrusives from the Goonumbla area, New South Gales. Australian Journal of Earth Sciences 48, 457–464.

Castiñeiras, P., 2005. Origen y evolución tectonotermal de las unidades de O Pino y Cariño (Complejos Alóctonos de Galicia). Nova Terra 28, 279 (In Spanish).

Chen, R.X., Zheng, Y.F., Xie, L., 2010. Metamorphic growth and recrystallization of zircon: Distinction by simultaneous in-situ analyses of trace elements, U–Th–Pb and Lu–Hf isotopes in zircons from eclogite-facies rocks in the Sulu orogen. Lithos 114, 132–154.

Coleman, D.S., Gray, W., Glazner, A.F., 2004. Rethinking the emplacement and evolution of zoned plutons: geochronologic evidence for incremental assembly of the Tuolumne Intrusive Suite, California. Geology 32, 433–436.

Corfu, F., Hanchar, J.M., Hoskin, P.W.O., Kinny, P., 2003. Atlas of zircon textures. In: Hanchar, J.M., Hoskin, P.W.O. (Eds.), Zircon. Reviews in Mineralogy and Geochemistry, 53. Mineralogical Society of America, Washington, pp. 468–500.

Dallmeyer, R.D., Martínez Catalán, J.R., Arenas, R., Gil Ibarguchi, J.I., Gutiérrez Alonso, G., Farias, P., Aller, J., Bastida, F., 1997. Diachronous Variscan tectonothermal activity in the NW Iberian Massif: evidence from $^{40}Ar/^{39}Ar$ dating of regional fabrics. Tectonophysics 277, 307–337.

Díaz García, F., Arenas, R., Martínez Catalán, J.R., González del Tánago, J., Dunning, G.R., 1999a. Tectonic evolution of the Careón Ophiolite (northwest Spain): a remnant of oceanic lithosphere in the Variscan Belt. Journal of Geology 107, 587–605.

Díaz García, F., Martínez Catalán, J.R., Arenas, R., González Cuadra, P., 1999b. Structural and kinematic analysis of the Corredoiras Detachment: evidence for early Variscan synconvergent extension in the Ordenes Complex, NW Spain. International Journal of Earth Sciences 88, 337–351.

Díaz García, F., Sánchez Martínez, S., Castiñeiras, P., Fuenlabrada, J.M., Arenas, R., 2010. A peri-Gondwanan arc in NW Iberia. II: assessment of the intra-arc tectonothermal evolution through the U–Pb SHRIMP dating of mafic dykes. Gondwana Research 17, 352–362.

Engels, J.P., 1972. The catazonal poly-metamorphic rocks of Cabo Ortegal (NW Spain), a structural and petrographic study. Leidse Geologische Mededelingen 48, 83–133.

Fernández Suárez, J., Arenas, R., Abati, J., Martínez Catalán, J.R., Whitehouse, M.J., Jeffries, T.E., 2007. U–Pb chronometry of polymetamorphic high-pressure granulites: an example from the allochthonous terranes of the NW Iberian Variscan belt. In: Hatcher Jr., R.D., Carlson, M.P., McBride, J.H., Martínez Catalán, J.R. (Eds.), 4-D Framework of Continental Crust: Geological Society of America Memoir, 200, pp. 469–488.

Fernández Suárez, J., Corfu, F., Arenas, R., Marcos, A., Martínez Catalán, J.R., Díaz García, F., Abati, J., Fernández, F.J., 2002. U–Pb evidence for a polymetamorphic evolution of the HP– HT units of the NW Iberia Massif. Contributions to Mineralogy and Petrology 143, 236–253.

Fernández Suárez, J., Díaz García, F., Jeffries, T.E., Arenas, R., Abati, J., 2003. Constraints on the provenance of the uppermost allochthonous terrane of the NW Iberian Massif: Inferences from detrital zircon U–Pb ages. Terra Nova 15, 138–144.

Fohey-Breting, N.K., Barth, A.P., Wooden, J.L., Mazdab, F.K., Carte, C.A., Schermer, E.R., 2010. Relationship of voluminous ignimbrites to continental arc plutons: petrology of Jurassic ignimbrites and contemporaneous plutons in southern California. Journal of Volcanology and Geothermal Research 189, 1–11.

Fuenlabrada, J.M., Arenas, R., Sánchez Martínez, S., Díaz García, F., Castiñeiras, P., 2010. A peri-Gondwanan arc in NW Iberia: I: isotopic and geochemical constraints to the origin of the arc — The sedimentary approach. Gondwana Research 17, 338–351.

Gagnevin, D., Daly, J.S., Kronz, A., 2010. Zircon texture and chemical composition as a guide to magmatic processes and mixing in a granitic environment and coeval volcanic system. Contributions to Mineralogy and Petrology, in press. doi:10.1007/s00410-009-0443-0.

Gil Ibarguchi, J.I., Ábalos., B., Azcarraga, J., 1999. Deformation, high-pressure metamorphism and exhumation of ultramafic rocks in a deep subduction/collision setting (Cabo Ortegal, NW Spain). Journal of Metamorphic Geology 17 (6), 747–764.

Gil Ibarguchi, J.I., Mendia, M., Girardeau, J., Peucat, J.J., 1990. Petrology of eclogites and clinopyroxene-garnet metabasites from the Cabo Ortegal Complex (northwestern Spain). Lithos 25, 133–162.

Gómez Barreiro, J., 2007. La Unidad de Fornás: Evolución tectonometamórfica del SO del Complejo de Órdenes. Nova Terra 32, 334 (In Spanish).

Gómez Barreiro, J., Martínez Catalán, J.R., Arenas, R., Castiñeiras, P., Díaz García, F., Wijbrans, J.R., 2007. Tectonic evolution of the upper allochthon of the Órdenes complex (northwestern Iberian Massif): structural constraints to a polyorogenic peri-Gondwanan terrane. In: Linneman, U., Nance, R.D., Kraft, P., Zulauf, G. (Eds.), The evolution of the Rheic Ocean: From Avalonian– Cadomian active margin to Alleghenian–Variscan collision: Geological Society of America Special Paper, 423, pp. 315–332.

Gómez Barreiro, J., Martínez Catalán, J.R., Prior, D., Wenk, H.-R., Vogel, S., Díaz García, F., Arenas, R., Sánchez Martínez, S., Lonardelli, I., 2010. Fabric Development in a Middle Devonian Intraoceanic Subduction Regime: the Careón Ophiolite (Northwest Spain). Journal of Geology 118, 163–186.

Gómez Barreiro, J., Wijbrans, J.R., Castiñeiras, P., Martínez Catalán, J.R., Arenas, R., Díaz García, F., Abati, J., 2006. $^{40}Ar/^{39}Ar$ laser probe dating of mylonitic fabrics in polyorogenic terrane of NW Iberia. Journal of the Geological Society of London 163, 61–73.

González Cuadra, P., 2007. La Unidad de Corredoiras (Complejo de Órdenes, Galicia): Evolución estructural y metamórfica. Serie Nova Terra 33, 254 (In Spanish).

Hanchar, J.M., van Westrenen, W., 2007. Rare earth element behavior in zircon–melt systems. Elements 3, 37–42.

Hoskin, P.W.O., 2005. Trace-element composition of hydrothermal zircon and the alteration of Hadean zircon from the Jack Hills, Australia. Geochimica et Cosmochimica Acta 69, 637–648.

Hoskin, P.W.O., Schaltegger, U., 2003. The composition of zircon and igneous and metamorphic petrogenesis. In: Hanchar, J.M., Hoskin, P.W.O. (Eds.), zircon. Reviews in Mineralogy and Geochemistry, 53. Mineralogical Society of America, Washington, pp. 27–62.

Iglesias, M., Choukroune, P., 1980. Shear zones in the Iberian arc. Journal of Structural Geology 2, 63–68.

Ireland, T.R., Williams, I.S., 2003. Considerations in zircon geochronology by SIMS. In: Hanchar, J.M., Hoskin, P.W.O. (Eds.), Zircon. Reviews in Mineralogy and Geochemistry, 53. Mineralogical Society of America, Washington, pp. 215–241.

Kellett, D.A., Grujic, D., Erdmann, S., 2009. Miocene structural reorganization of the South Tibetan detachment, eastern Himalaya: implications for continental collision. Lithosphere 1, 259–281. doi:10.1130/L56.1.

Kempe, U., Gruner, T., Nasdala, L., Wolf, D., 2000. Relevance of cathodoluminescence for the interpretation of U–Pb zircon ages, with an example of an application to a study of zircons from the Saxonian Granulite Complex, Germany. In: Pagel, M., Barbin, V., Blanc, P., Ohnenstetter, D. (Eds.), Cathodoluminescence in Geosciences. Springer, Berlin, pp. 425–455.

Korotev, R.L., 1996. A self-consistent compilation of elemental concentration data for 93 geochemical reference samples. Geostandards Newsletter 20, 217–245.

Linnemann, U., Pereira, F., Jeffries, T.E., Drost, K., Gerdes, A., 2008. The Cadomian Orogeny and the opening of the Rheic Ocean: the diachrony of geotectonic processes constrained by IA-ICP-MS U–Pb zircon dating (Ossa-Morena and Saxo-Thuringian Zones, Iberian and Bohemian Massifs). Tectonophysics 461, 21–43.

Lowery Claiborne, L., Miller, C.F., Walker, B.A., Wooden, J.L., Mazdab, F.K., Bea, F., 2006. Tracking magmatic processes through Zr/Hf ratios in rocks and Hf and Ti zoning in zircons: an example from the Spirit Mountain batholith, Nevada. Mineralogical Magazine 70, 517–543.

Ludwig, K.R., 2002. SQUID 1.02, a user's manual. Berkeley Geochronology Center Special Publication 2, 17.

Ludwig, K.R., 2003. ISOPLOT/Ex, version 3, a geochronological toolkit for Microsoft Excel. Berkeley Geochronology Center Special Publication 4, 71.

Ludwig, K.R., Mundil, R., 2002. Extracting reliable U–Pb ages and errors from complex populations of zircons from Phanerozoic tuffs. Geochimica et Cosmochimica Acta 66, 463.

Martínez Catalán, J.R., Arenas, R., Abati, J. Sánchez, Martínez, S., Díaz García, F., Fernández Suárez, J., González Cuadra, P., Castiñeiras, P., Gómez Barreiro, J., Díez Montes, A., González Clavijo, E., Rubio Pascual, F.J., Andonaegui, P., Jeffries, T.E., Alcock, J.E., Díez Fernández, R., López, Carmona A., 2009. A rootless suture and the

lost roots of a mountain chain: the Variscan belt of NW Iberia. Comptes Rendus Geoscience 341, 114–126.

Martínez Catalán, J.R., Arenas, R., Díaz García, F., González Cuadra, P., Gómez- Barreiro, J., Abati, J., Castiñeiras, P., Fernández-Suárez, J., Sánchez Martínez, S., Andonaegui, P., González Clavijo, E., Díez Montes, A., Rubio Pascual, F.J., Valle Aguado, B., 2007. Space and time in the tectonic evolution of the northwestern Iberian Massif: implications for the Variscan belt. In: Hatcher Jr., R.D., Carlson, M.P., McBride, J.H., Martínez Catalán, J.R. (Eds.), 4-D Framework of Continental Crust: Geological Society of America Memoir, 200, pp. 403–423.

Martínez Catalán, J.R., Díaz García, F., Arenas, R., Abati, J., Castiñeiras, P., González Cuadra, P., Gómez Barreiro, J., Rubio Pascual, F., 2002. Thrust and detachment systems in the Órdenes Complex (northwestern Spain): implications for the Variscan–Appalachian geodynamics. In: Martínez Catalán, J.R., Hatcher Jr., R.D., Arenas, R., Díaz García, F. (Eds.), Variscan– Appalachian Dynamics: the building of the Late Paleozoic Basement: Geological Society of America Special Paper, 364, pp. 163–182.

Mattinson, C.G., Wooden, J.L., Zhang, J.X., Bird, D.K., 2009. Paragneiss zircon geochronology and trace element geochemistry, North Qaidam HP/UHP terrane, western China. Journal of Asian Earth Sciences 35, 298–309.

McClelland, W.C., Power, S.E., Gilotti, J.A., Mazdab, F.K., Wopenka, B., 2006. U–Pb SHRIMP geochronology and trace-element geochemistry of coesite-bearing zircons, North-East Greenland Caledonides. In: Hacker, B.R., McClelland, W.C., Liou, J.G. (Eds.), Ultrahigh-pressure metamorphism: Deep continental subduction: Geological Society of America, Boulder. Geological Society of America Special Paper, 403, pp. 23–43.

Moreno, T., Gibbons, W., Prichard, H.M., Lunar, R., 2001. Platiniferous chromitite and the tectonic setting of ultramafic rocks in Cabo Ortegal, NW Spain. Journal of the Geological Society 158, 601–614.

Murphy, J.B., Gutiérrez Alonso, G., Nance, R.D., Fernández-Suárez, J., Keppie, J.D., Quesada, C., Strachan, R.A., Dostal, J., 2006. Origin of the Rheic Ocean: rifting along a Neoproterozoic suture? Geology 34, 325–328.

Murphy, J.B., Keppie, J.D., Nance, R.D., Dostal, J., 2010. Comparative evolution of the Iapetus and Rheic Oceans: a North America perspective. Gondwana Research 17, 482–499. doi:10.1016/j.gr.2009.08.009.

Nance, R.D., Gutiérrez-Alonso, G., Keppie, J.D., Linnemann, U., Murphy, J.B., Quesada, C., Strachan, R.A., Woodcock, N.H., 2010. Evolution of the Rheic Ocean. Gondwana Research, in press. doi:10.1016/j.gr.2009.08.001.

Ordoñez Casado, B., Gebauer, D., Schäfer, H.J., Gil Ibarguchi, J.I., Peucat, J.J., 2001. A single Devonian subduction event for the HP/HT metamorphism of the Cabo Ortegal complex within the Iberian Massif. Tectonophysics 332, 359–385.

Peucat, J.J., Bernard-Griffiths, J., Gil Ibarguchi, J.I., Dallmeyer, R.D., Menot, R.P., Cornichet, J., Ponce, Iglesias, de León, M., 1990. Geochemical and geochronological cross section of the deep Variscan crust: the Cabo Ortegal high-pressurenappe (northwestern Spain). Tectonophysics 177, 263–292.

Puelles, P., Ábalos, B., Gil Ibarguchi, J.I., 2005. Metamorphic evolution and thermobaric structure of the subduction-related Bacariza high-pressure granulite formation (Cabo Ortegal Complex, NW Spain). Lithos 84, 125–149.

Ribeiro, A., Munha, J., Dias, R., Mateus, A., Pereira, E., Ribeiro, L., Fonseca, P., Araujo, A., Oliveira, T., Romao, J., Chamine, H., Coke, C., Pedro, J., 2007. Geodynamic evolution of the SW Europe Variscides. Tectonics 26, 1–24.

Roger, F., Matte, Ph., 2005. Early Variscan HP metamorphism in the western Iberian Allochthon. A 390 Ma U–Pb age for the Bragança eclogite (NW Portugal). International Journal of Earth Sciences 94, 173–179.

Rubatto, D., 2002. Zircon trace element geochemistry: partitioning with garnet and the link between U–Pb ages and metamorphism. Chemical Geology 184, 123–138.

Rubatto, D., Gebauer, D., 2000. Use of cathodoluminescence for U–Pb zircon dating by ion microprobe: some examples from the Western Alps. In: Pagel, M., Barbin, V., Blanc, P., Ohnenstetter, D. (Eds.), Cathodoluminescence in Geosciences. Springer, Berlin, pp. 373–400.

Sánchez Martínez, S., Arenas, R., Díaz García, S., Martínez Catalán, J.R., Gómez Barreiro, J., Pearce, J., 2007. The Careón Ophiolite, NW Spain: supra- subduction zone setting for the youngest Rheic Ocean floor. Geology 35, 53–56.

Santos Zalduegui, J.F., Schärer, U., Gil Ibarguchi, J.I., Girardeau, J., 1996. Origin and evolution of the Paleozoic Cabo Ortegal ultramafic–mafic complex (NW Spain): U–Pb, Rb–Sr and Pb–Pb isotope data. Chemical Geology 129, 281–304.

Santos Zalduegui, J.F., Schärer, U., Gil Ibarguchi, J.I., Girardeau, J., 2002. Genesis of pyroxenite-rich peritotite at Cabo Ortegal (NW Spain): geochemical and Pb–Sr–Nd isotope data. Journal of Petrology 43, 17–43.

Schäfer, H.G., Gebauer, D., Gil Ibarguchi, J.I., Peucat, J.J., 1993. Ion-microprobe U–Pb zircon dating on the HP/Ht Cabo Ortegal Complex (Galicia, NW Spain): preliminary results. Terra Abstracts 5 (4), 22.

Stacey, J.S., Kramers, J.D., 1975. Approximation of terrestrial lead isotope evolution by a two-stage model. Earth and Planetary Science Letters 26, 207–221.

van Calsteren, P.W.C., Boelrijk, N.A.I.M., Hebeda, E.H., Priem, H.N.A., Den Tex, E., Verdurmen, E.A.T., Verschure, R.H., 1979. Isotopic dating of older elements (including the Cabo Ortegal mafic–ultramafic complex) in the Hercynian orogen of NW Spain: manifestations of a presumed early Palaeozoic mantle-plume. Chemical Geology 24, 35–56.

Vavra, G., Gebauer, D., Schmid, R., Compston, W., 1996. Multiple zircon growth and recrystallization during polyphase Late Carboniferous to Triassic metamorphism in granulites of the Ivrea Zone (Southern Alps): an ion microprobe (SHRIMP) study. Contributions to Mineralogy and Petrology 122, 337–358.

von Raumer, J.F., Stampfli, G.M., 2008. The birth of the Rheic Ocean–Early Palaeozoic subsidence patterns and subsequent tectonic plate scenarios. Tectonophysics 461, 9–20.

Whitehouse, M.J., Platt, J.P., 2003. Dating high-grade metamorphism-constraints from rare-earth elements in zircon and garnet. Contributions to Mineralogy and Petrology 145, 61–74.

Williams, I.S., 1997. U–Th–Pb geochronology by ion microprobe: not just ages but histories. Economic Geology 7, 1–35.

Wooden, J.L., Mazdab, F.K., Barth, A.P., Miller, C.F., Lowery, L.E., 2006. Temperatures (Ti) and compositional characteristics of zircon: early observations using high mass resolution on the USGS-Stanford SHRIMP-RG. Third SHRIMP workshop, Rottnest Island, Australia. Program and abstracts 64–65.

Yui, T.F., Okamoto, K., Usuki, T., Lan, C.Y., Liou, J.G., 2009. Triassic–Jurassic accretion/subduction in Taiwan region along the SE margin of South China: evidence from zircon SHRIMP dating. International Geology Review 51, 304–328.